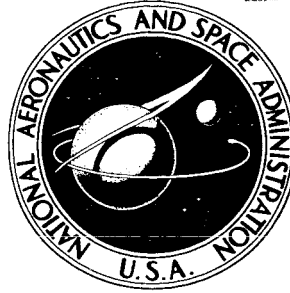


67 15401

Available from NASA to U. S.
Government agencies and U. S.
Government contractors only.

**NASA TECHNICAL
MEMORANDUM**



UB
NASA TM X-1336

~~SECRET~~

Declassified by authority of NASA
Classification Change Notices No. 218
Dated 30 SEP 1972

CLASSIFICATION CHANGED
UNCLASSIFIED

By Authority of 7072235 Date 6/8/72

UB
NASA TM X-1336

**CASE FILE
COPY**

**TRANSONIC AERODYNAMIC CHARACTERISTICS
OF A POWERED WIND-TUNNEL MODEL
OF THE APOLLO LAUNCH-ESCAPE VEHICLE
DURING SEPARATION**

by Bobby L. Berrier and Odis C. Pendergraft, Jr.

Langley Research Center

Langley Station, Hampton, Va.

NATIONAL AERONAUTICS AND SPACE ADMINISTRATION • WASHINGTON, D. C. • APRIL 1967

TRANSONIC AERODYNAMIC CHARACTERISTICS OF A POWERED
WIND-TUNNEL MODEL OF THE APOLLO LAUNCH-ESCAPE
VEHICLE DURING SEPARATION

By Bobby L. Berrier and Odis C. Pendergraft, Jr.

Langley Research Center
Langley Station, Hampton, Va.



CLASSIFIED DOCUMENT-TITLE UNCLASSIFIED
This material contains information affecting the
national defense of the United States within the
meaning of the espionage laws, Title 18, U.S.C.,
Secs. 793 and 794, the transmission or revelation
of which in any manner to an unauthorized person
is prohibited by law.

NOTICE
This document should not be returned after
satisfaction. It may be disposed
of in accordance with the security regula-
tions or the approval of the Industrial
Security Manual for Safe-Guarding Classified
Information.

NATIONAL AERONAUTICS AND SPACE ADMINISTRATION

[REDACTED]

TRANSONIC AERODYNAMIC CHARACTERISTICS OF A POWERED
WIND-TUNNEL MODEL OF THE APOLLO LAUNCH-ESCAPE
VEHICLE DURING SEPARATION*

By Bobby L. Berrier and Odis C. Pendergraft, Jr.
Langley Research Center

SUMMARY

An investigation of a model of the Apollo launch-escape vehicle in close proximity to the service module has been made at Mach numbers from 0.70 to 1.10. By changing the attitude of the service module relative to the command module, ten different configurations were investigated. The longitudinal distance between the service module and command module was varied for each configuration. The escape-rocket exhaust was simulated with a hydrogen peroxide rocket mounted upstream of the command module. The angle-of-attack range was 0° to 15° , and the average Reynolds number based on the maximum command-module diameter was 4.34×10^6 at a Mach number of 0.90.

The results of the investigation indicate that the axial force (drag), and thus the escape-rocket thrust margin, depends to a large extent on the trajectory traced by the launch-escape vehicle as it separates from the service module. The axial force (drag) of the launch-escape vehicle is greatly increased for small initial longitudinal displacements of the service module downstream of the command module; however, any further longitudinal displacement of the service module resulted in a decrease of axial force of the launch-escape vehicle. It was also found that displacing the service module vertically while in close proximity to the command module decreased axial force (drag) on the launch-escape vehicle.

INTRODUCTION

To provide a means of escape in the event of a malfunction during the launch phase of Project Apollo, an escape rocket mounted to the Apollo command module, similar to that used for Project Mercury, is provided to separate the command module and its crew from the service module and booster. (See ref. 1.) A wind-tunnel investigation of the effects of rocket-exhaust gas on the aerodynamic characteristics of the Apollo launch-escape vehicle is reported in reference 2 where the launch-escape vehicle was assumed to be far enough away from the booster to be free of any flow-field interference effects. However, no information has been published concerning the effect of the service module on

[REDACTED]

[REDACTED]

the aerodynamic characteristics of the launch-escape vehicle during separation. Therefore an investigation was conducted to determine the aerodynamic characteristics of a 0.085-scale model of the launch-escape vehicle while in close proximity to the service module.

Ten service-module configurations of different pitch attitudes and vertical displacements relative to the command module were investigated at several axial-separation distances. Tests were conducted at Mach numbers from 0.70 to 1.10, at angles of attack from 0° to 15° , and at ratios of rocket-chamber pressure to free-stream static pressure from 1.0 (jet off) to 186.0. A hydrogen peroxide gas generator was used to provide hot exhaust gas to simulate the escape-rocket operation. For further information concerning the rocket-exhaust simulation, see reference 2.

SYMBOLS

The positive direction of forces and moments is shown in figure 1. The basic data presented herein are referred to the body system of axes with the origin located at the theoretical apex of the command module.

| | |
|------------------|--|
| A | reference area, maximum cross-sectional area of command module, 868.2331 sq cm |
| d | maximum diameter of command module, 33.25 cm |
| l | length of command module measured from apex, 30.78 cm |
| M | free-stream Mach number |
| p | pressure, N/m^2 |
| p_j | rocket-chamber pressure, N/m^2 |
| q | dynamic pressure, N/m^2 |
| r | radius, m |
| x | longitudinal distance from apex, positive rearward, m (see fig. 6) |
| Δx | longitudinal displacement, measured from maximum diameter of command module to front-face center line of service module, positive rearward, m (see fig. 2) |
| Δz | vertical displacement, measured from longitudinal axis of command module to front-face center line of service module, positive downward, m (see fig. 2) |
| $\Delta\alpha_s$ | relative angle of attack between command module and service module, positive clockwise, deg (see fig. 2) |

- α angle of attack of model center line, deg
- ϕ angular location of orifice with respect to module longitudinal axis, positive in counterclockwise direction looking upstream, deg (see fig. 6)
- θ angle between model center line and thrust axis, deg

Subscripts:

- a ambient
- av average
- b base
- j jet
- l local
- ∞ free stream

Coefficients

Aerodynamic coefficients (includes jet-interference effects but not the direct forces or moments produced by the jets):

- C_A axial-force coefficient, $\frac{\text{Axial force}}{q_{\infty} A}$
- C_m pitching-moment coefficient, $\frac{\text{Pitching moment}}{q_{\infty} A d}$
- C_N normal-force coefficient, $\frac{\text{Normal force}}{q_{\infty} A}$

Coefficients of force and moment components of jet thrust:

- $C_{A,f}$ static axial-thrust coefficient, $\frac{(\text{Axial force})_j}{p_a A}$
- $C_{A,j}$ thrust coefficient, $\frac{(\text{Axial force})_j}{q_{\infty} A \cos 35^\circ}$
- C_j resultant thrust coefficient, $\frac{C_{A,f}}{\cos \theta}$ or $\frac{C_{A,j} \cos 35^\circ}{\cos \theta}$

~~CONFIDENTIAL~~

$C_{m,f}$ static pitching-moment coefficient, $\frac{(\text{Pitching moment})_j}{p_a A_d}$

$C_{m,j}$ pitching-moment coefficient, $\frac{(\text{Pitching moment})_j}{q_\infty A_d}$

$C_{N,f}$ static normal-force coefficient, $\frac{(\text{Normal force})_j}{p_a A}$

$C_{N,j}$ normal-force coefficient, $\frac{(\text{Normal force})_j}{q_\infty A}$

Coefficients with aerodynamic and thrust components included:

$C_{A,t}$ total axial-force coefficient, $C_A - C_{A,j} \cos 35^\circ$

$C_{m,t}$ total pitching-moment coefficient, $C_m + C_{m,j}$

$C_{N,t}$ total normal-force coefficient, $C_N + C_{N,j}$

Pressure coefficient:

C_p pressure coefficient, $\frac{p_l - p_\infty}{q_\infty}$

APPARATUS AND PROCEDURE

Wind Tunnel

This investigation was conducted in the Langley 16-foot transonic tunnel (4.88 m), which is a single-return atmospheric wind tunnel with an octagonal slotted test section and continuous air exchange. It has a speed range from a Mach number of 0.30 to 1.30, and the Mach number is varied by changing the rotational speed of the drive fans.

Model and Support System

A sketch of the Apollo launch-escape vehicle, service module, and sting support is shown in figure 2. Photographs of the model installed in the test

[REDACTED]

section of the Langley 16-foot transonic tunnel (4.88 m) are shown in figures 3 and 4. The model consisted of the escape-rocket simulator, rocket-support structure, command module, and a service module attached to the sting-support system.

The sting-support system actually consisted of three different stings used during the separate phases of this investigation. These three stings are shown in figure 2. Sting 1 has a diameter of 16.61 cm and a gap between the sting and command module of 1.52 cm. Sting 2 has the same diameter as sting 1 but the gap is increased to 5.08 cm. Sting 3 has a nominal diameter of 6.81 cm and has no gap between the sting and the command module. Sting 3 was used to support the launch-escape vehicle, while stings 1 and 2 were built up around sting 3 and were used as a bearing surface for the movable service-module configurations.

The service module used with sting 1 was motorized so that the longitudinal distance from the command module to the front face of the service module, as denoted by Δx , could be controlled remotely. Ten different service-module configurations were obtained by attaching the service module to the sting track at fixed values of Δz and $\Delta \alpha_s$. Figure 2 presents a list of configurations giving the range of $\Delta x/d$ and the values of $\Delta z/d$ and $\Delta \alpha_s$ used during the test. Different configurations were obtained while using sting 2 by setting fixed values of $\Delta x/d$, $\Delta z/d$, and $\Delta \alpha_s$ before each run. The service module was not used with sting 3.

The launch-escape vehicle was attached to sting 3 through a six-component strain-gage balance located in the command module. The service module was not attached to the balance.

A hydrogen peroxide gas generator located in the escape rocket was used to produce hot rocket exhaust. Details of this arrangement are shown in figure 5. A more detailed description of the catalyst pack, escape rocket, and propellant-supply system may be found in reference 2. Typical hydrogen peroxide hot-jet simulators and the related propellant-supply system are described in reference 3. The liquid hydrogen peroxide was piped through the sting and rocket-tower structure into a radial-flow catalyst pack located in the escape rocket. The propellant lines entered the model and passed over the balance in a flexible helix restraint system so that restraint on the balance was held to a minimum. (See ref. 2.) The resulting exhaust products, oxygen and superheated steam (1011°K), were exhausted through four nozzles located at the rocket base and canted outward 35° . The model rocket nozzles had scaled throat and exit areas and the same expansion ratios as the full-scale rocket nozzles. The two nozzles in the yaw plane had equal throat areas and equal exit-area ratios of 8.59. The top nozzle in the pitch plane had a smaller throat area and a larger exit-area ratio of 10; the lower pitch nozzle had a larger throat area and smaller exit-area ratio of 7.62. The asymmetric thrust of the pitch nozzles provided the offset thrust vector (2045°) shown in figure 1.

Instrumentation

A sketch showing pressure-orifice locations is given in figure 6. Pressures were measured at several radial angles around the command and service modules. Pressures were also measured at several radial angles on the command-module base. In addition, pressures were measured in the rocket-exhaust plenum chamber as indicated in figure 5. The pressure tubing from each orifice was connected through the sting barrel to an electrical pressure transducer. The electrical pressure transducers were connected to a common reference pressure.

Forces and moments on the model were measured by a six-component strain-gage balance. Liquid hydrogen peroxide flow was measured with a vane type of electronic flowmeter located in the hydrogen peroxide supply line.

Tests

This investigation covered a Mach number range from 0.70 to 1.10 and angles of attack from 0° to 15° . Data were obtained through a range of rocket exhaust total pressure to free-stream static-pressure ratios from 1.0 (jet off) to 186.0. The average Reynolds number based on the maximum command-module base diameter was 4.34×10^6 at a Mach number of 0.90. All configurations were tested at $M = 0.90$ and several were tested at $M = 0.70$ and $M = 1.10$ to determine Mach number effects. From previous Apollo tests with the service module, this Mach number range was determined to represent minimum thrust-minus-drag conditions, with $M = 0.90$ representing the worst conditions. Ten different configurations were tested by setting fixed values of Δz and $\Delta \alpha_s$ before each run and then varying Δx remotely during the run.

Data Reduction

Electrical signals from the pressure transducers, balance, and flowmeters were recorded on tape as millivolt readings. The pressures and forces were converted to standard pressure and force coefficients, and the electronic flowmeter signal was converted to kilograms per second by machine computation from the millivolt readings.

All aerodynamic coefficients in this report have all applicable components of the jet thrust removed, as follows:

$$C_A = C_{A,t} + C_{A,j} \cos 35^\circ$$

$$C_m = C_{m,t} - C_{m,j}$$

$$C_N = C_{N,t} - C_{N,j}$$

[REDACTED]

This calculation removes all force and moment components due to jet thrust but retains all jet-exhaust interference effects on the command-module pressures and aerodynamic characteristics.

The components of axial force ($C_{A,f}$), normal force ($C_{N,f}$), and pitching moment ($C_{m,f}$) due to the rocket thrust were obtained from a static calibration. Figure 7 presents the variation of $C_{A,f}$, $C_{N,f}$, and $C_{m,f}$ with rocket-chamber pressure ratio. The command module was covered with a shroud, which was not attached to the balance, to prevent measurement of any jet forces on the command module during the static tests. The jet-thrust coefficient was obtained by dividing the jet axial-force coefficient obtained from static calibrations by the cosine of the nozzle cant angle (35°):

$$C_{A,j} = \frac{(\text{Axial force})_j}{q_\infty A \cos 35^\circ} \quad \text{or} \quad \frac{(\text{Axial force})_j}{p_a A \cos 35^\circ}$$

RESULTS AND DISCUSSION

Support Interference Effects

The investigation of the Apollo launch-escape vehicle was separated into several different phases. In order to attach the service module and its remote-control mechanism behind the command module, a larger sting was required for the separation test phase than for the other phases. The service module was used with stings 1 and 2 while sting 3 was used for the launch-escape vehicle without the service module. These stings are indicated in figure 2. It is possible to indicate the effect of the larger stings by comparing the base pressures on the command module for each sting.

Figures 8(a) and 8(b) show a comparison of the command-module base pressures when stings 1 and 3 were used at Mach numbers of 0.90 and 1.10, respectively. The base pressures associated with sting 3 are lower than those associated with sting 1 for all conditions of Mach number, angle of attack, and jet-thrust coefficient shown. The maximum difference between base-pressure coefficients associated with these two stings at a Mach number of 0.90 is approximately 0.1. This difference is decreased to a value of 0.03 at $\alpha = 15^\circ$. Increasing Mach number generally increases the difference between the base-pressure coefficients associated with these two support systems.

The effect of stings 1 and 2 on the command-module base pressures is shown in figure 9. The command-module base pressures associated with sting 1 are lower than those associated with sting 2 at the lower angles of attack; however, at $\alpha = 10^\circ$, this trend is reversed.

It is shown in figures 8 and 9 that, in general, the command-module base pressures associated with the smaller sting (3) are lower than the base pressures associated with the larger stings (1 and 2). All data shown in this

[REDACTED]

report were obtained with either sting 1 or sting 2 unless otherwise stated. Thus, the absolute drag levels shown herein, obtained with larger stings, appear to be too low when compared with data obtained with a smaller sting. This effect is shown in reference 4 for all rear sting-supported slender bodies. It is clear that base drag depends on the diameter of the rear support and that such sting effects are certainly present in the data presented in the following sections. Due to the limited amount of data published about sting effects on a blunt body in the transonic speed regime and the limited amount of data shown herein, any attempt to correct or extrapolate the data would be unrealistic. However, it is believed that the relative magnitudes of base pressures and base drag are useful in determining trends in the aerodynamic characteristics of the command module as the service-module attitude is changed while all other test variables are held constant (e.g., M , α , and sting size).

Typical Pressure Distributions

The variation of pressure coefficients with the ratio x/l is shown in figures 10 and 11. Pressure coefficients for the command-module surface, command-module base, and service-module surface are shown for a radial angle of 0° ($\phi = 0^\circ$) and several values of the ratio $\Delta x/d$ in figures 10(a) and 10(b). Changing the spacing ratio $\Delta x/d$ has little effect on the command-module surface pressures. The command-module base pressures however are greatly decreased for small initial longitudinal displacements as the service module separates from the command module. The command-module base pressures and the service-module surface pressures increase for any further longitudinal displacement of the service module downstream of the command module for both jet-on and jet-off conditions. The highest base pressures occur for $\Delta x/d = \infty$ or with no service module. Operation of the escape rocket increases most of the surface pressures on the conical face of the command module and decreases the pressures on the command-module base and service-module surface.

Figure 11(a) presents pressure distributions for $\phi = 180^\circ$ and several values of the ratio $\Delta z/d$. The command-module conical-surface pressures generally increase with increasing $\Delta z/d$ for both jet-off and jet-on conditions. The command-module base pressures varied over a wide range of values and are discussed in a subsequent section of this report. Operation of the escape rocket generally increases the pressures on the command-module conical surface and decreases the pressures on the command-module base for all values of $\Delta z/d$.

Figure 11(b) presents pressure distributions for $\phi = 180^\circ$ and several values of $\Delta \alpha_s$. Changing $\Delta \alpha_s$ has little or no effect on the command-module conical-surface pressures. Addition of the service module produces a large decrease in the base pressures for both jet-on and jet-off conditions. However, varying $\Delta \alpha_s$ had very little effect on the base pressures. Operation of the escape rocket again produces an increase in most of the command-module conical-surface pressures and a decrease in command-module base pressures.

The pressure distributions at several radial angles around the command module are shown in figure 11(c). The flow around the model is symmetrical for the jet-off condition; however, some disturbance of the flow field is noted for

[REDACTED]

the jet-on case. Operation of the escape rocket increases most of the pressures on the command-module conical surface.

Figure 11(d) presents the pressure distributions on the command module at $\phi = 180^\circ$ for several angles of attack. More complete pressure distributions on the command-module conical surface are given in reference 2. Increasing the angle of attack generally increases the pressure coefficients on the command-module conical surface for $\phi = 180^\circ$. Escape-rocket operation tends to diminish the effect of angle of attack. Base-pressure coefficients for the jet-off case are decreased with increasing angle of attack while no evident trends are shown for the jet-on case.

Base-Pressure Data

Effect of $\Delta x/d$. Figure 12 presents the variation of the average base-pressure coefficients with the spacing ratio $\Delta x/d$ for several angles of attack and thrust coefficients.

During initial separation of the command module from the service module, the base region is strongly aspirated and produces very low base pressures. The lowest values of base pressures are obtained in the range of $\Delta x/d$ from 0.01 to 0.10. It should be noted that the data fairing in this range of $\Delta x/d$ was determined from data using sting 2. An example is shown for $\alpha = 0^\circ$ and $C_{A,j} = 0$. The data from sting 2, however, do not agree exactly with the data using sting 1, as a result of differences in sting-interference effects, but the data do indicate base-pressure trends in the range of $\Delta x/d$ of 0.013 to 0.25. After the lowest value of base-pressure coefficient is reached during separation, any further increase of $\Delta x/d$ increases the base pressures. Operation of the escape rocket generally decreases the base pressures at all angles of attack.

Effect of $\Delta z/d$. Pressure distributions around the command-module base are shown in figure 13 for several values of angle of attack, jet thrust coefficient, and $\Delta z/d$. A value for $\Delta x/d$ of 0.20 was chosen since this value represents very low base pressures as shown in figure 12 and thus represents values near maximum drag or minimum thrust margin. Base pressures increase as the ratio $\Delta z/d$ increases for all values of angle of attack and jet thrust coefficient. This favorable effect of reducing base drag, and thus increasing thrust margin, in a critical region of $\Delta x/d$ is probably a result of the scooping effect of the service module as it is displaced into the free stream. Air is scooped from the free stream into the base region by the front face of the service module, and thus tends to pressurize the base region between the command-module base and service-module front face.

Operation of the escape rocket generally tends to decrease the base pressures, while increasing angle of attack generally increases the base pressures.

Effect of $\Delta \alpha_s$. Figures 14(a) and 14(b) present the effects of changing $\Delta \alpha_s$ on the pressure distributions around the command-module base for values of $\Delta z/d$ of 0 and 0.20, respectively, and at several values of angle of attack

[REDACTED]

[REDACTED]

and jet thrust coefficient. Figure 14(a) shows that the overall levels of base-pressure coefficients are affected only slightly at $\alpha = 0^\circ$ when compared with the large effects already shown for $\Delta x/d$ and $\Delta z/d$. However, at $\alpha = 10^\circ$ the effect of varying $\Delta\alpha_s$ is more pronounced. The base-pressure coefficients became less negative when the service module was rotated to $\Delta\alpha_s = 10^\circ$.

Figure 14(b) shows very little effect of varying $\Delta\alpha_s$ on the overall levels of base pressure when the service module is given an initial vertical displacement of $\Delta z/d = 0.20$. The large effect of vertical displacement of the service module on the command-module base pressures, as shown in figure 13, probably overshadows any small effect that changes in $\Delta\alpha_s$ have on the base pressures.

In general, the effect of $\Delta\alpha_s$ on the command-module base pressures is small when compared with the large effects of $\Delta x/d$ and $\Delta z/d$ on the base pressures. This effect is particularly true for $\alpha = 0^\circ$ or when the service module has an initial vertical displacement, as denoted by $\Delta z/d$.

Force and Moment Characteristics

Effect of $\Delta x/d$.— The effect of the ratio $\Delta x/d$ on C_A , C_N , and C_m for various values of $\Delta z/d$, $\Delta\alpha_s$, α , and $C_{A,j}$ is shown in figure 15. The variations of axial force with the ratio $\Delta x/d$ are shown in figure 15(a) for $\Delta z/d$ and $\Delta\alpha_s$ equal to zero. It should be noted that C_A is positive in the drag direction (see fig. 1) and is equal to the drag coefficient at $\alpha = 0^\circ$. The maximum value of C_A occurs for a spacing ratio, $\Delta x/d$, between 0.01 and 0.10. This value occurs at conditions where the most negative base-pressure coefficients are noted, in figure 12, and is associated with the high base drag produced by these pressures. The data fairing in this region of $\Delta x/d$ was determined from data from tests using sting 2. An example is shown for $\alpha = 0^\circ$ and $C_{A,j} = 0$. As a result of different sting-interference effects, the level of the data obtained with sting 2 differs from that of sting 1 but does indicate a trend for fairing in the region of $\Delta x/d$ between 0.01 and 0.25. Any further increase in the ratio $\Delta x/d$, after the maximum value of C_A is obtained, rapidly decreases C_A . This effect of $\Delta x/d$ on C_A was indicated by the effect of $\Delta x/d$ on the command-module base pressures. Although operation of the escape rocket increases the axial-force coefficient for all angles of attack shown, the effect of $\Delta x/d$ remains essentially the same regardless of escape-rocket operation or angle of attack.

The coefficients C_N and C_m are presented in figure 15(b) plotted against $\Delta x/d$ for $\Delta z/d = 0$ and $\Delta\alpha_s = 0^\circ$ and for several values of angle of attack and jet thrust coefficient. Although variations of thrust coefficient and angle of attack change the level of C_N and C_m , varying $\Delta x/d$ has little effect on either C_N or C_m .

[REDACTED]

In figure 15(c), C_A , C_N , and C_m are shown plotted against $\Delta x/d$ for $\Delta z/d = 0.20$ and $\Delta \alpha_s = 0^\circ$. Axial-force coefficient increases with increasing $\Delta x/d$, and the effect of $\Delta x/d$ on C_A is therefore reversed when $\Delta z/d$ is increased from 0.0 to 0.20, as shown in figures 15(a) and 15(c). Therefore, it is apparent that the effect of $\Delta x/d$ on the axial-force coefficient is dependent on the vertical displacement of the service module. For $\Delta z/d = 0.20$, the increase in C_A when the service module is displaced longitudinally may be explained by the fact that $\Delta z/d$ has a large favorable effect on C_A , as is shown in a later section of this report, and this favorable effect becomes smaller as $\Delta x/d$ increases.

The effect of $\Delta x/d$ on C_N and C_m is greater when the service module is displaced downward than the effect of $\Delta x/d$ for the symmetrical configuration, although both effects are relatively small.

Changes in angle of attack and escape-rocket operation affect the levels of C_A , C_N , and C_m but do not greatly alter the effect of increasing $\Delta x/d$ on these coefficients.

Figure 15(d) presents the variations of C_A , C_N , and C_m with $\Delta x/d$ for $\Delta z/d = 0$ and $\Delta \alpha_s = 10^\circ$. As with $\Delta \alpha_s = 0^\circ$, the axial-force coefficient rapidly decreases with increasing $\Delta x/d$. Thus, it appears that the effect of $\Delta x/d$ is not dependent to any significant extent on the value of $\Delta \alpha_s$ as it is on the value of $\Delta z/d$.

No significant effect is noted on either the normal-force coefficient or the pitching-moment coefficient when $\Delta x/d$ is varied and $\Delta \alpha_s = 10^\circ$.

Increasing angle of attack generally decreases C_A and C_m and increases C_N , and operation of the escape rocket increases C_A and C_m and decreases C_N for both angles of attack shown; however, the effect of increasing $\Delta x/d$ on C_A , C_N , and C_m remains essentially the same regardless of escape-rocket operation or angle of attack.

Figure 16 presents the variations of axial-force coefficient with $\Delta x/d$ for various combinations of $\Delta z/d$ and $\Delta \alpha_s$. In general, the axial-force coefficient decreases with increasing $\Delta x/d$ when the service module is not displaced vertically ($\Delta z/d = 0$) regardless of the value of $\Delta \alpha_s$. However, when the service module is displaced vertically ($\Delta z/d \neq 0$), any increase in $\Delta x/d$ generally increases the axial-force coefficient, which may reach a maximum value and then decrease, depending on the value of $\Delta \alpha_s$.

In general, the effect of $\Delta x/d$ depends largely on the value of $\Delta z/d$ and to a lesser degree on the value of $\Delta \alpha_s$. With increasing $\Delta x/d$, the axial-force coefficient usually approaches the value corresponding to the condition where the command module is not influenced by the presence of the service module ($\Delta x/d = \infty$).

[REDACTED]

[REDACTED]

Effect of $\Delta z/d$. - The variations of C_A , C_N , and C_m with $\Delta z/d$ are shown in figure 17 for two different values of $\Delta x/d$.

For $\Delta x/d = 0.20$, the axial-force coefficient rapidly decreases with increasing $\Delta z/d$. The decrease in axial-force coefficient is associated with the large increase in command-module base pressures with increasing $\Delta z/d$, thus decreasing base drag and axial-force coefficient. The variations of C_N and C_m with $\Delta z/d$ are presented in figure 17(b); C_N and C_m are only slightly affected by increasing $\Delta z/d$.

Although operation of the escape rocket and increasing angle of attack changes the level of C_A , C_N , and C_m , the trends of C_A , C_N , and C_m with increasing $\Delta z/d$ do not appreciably change.

Figures 17(c) and 17(d) give the variation of C_A , C_N , and C_m with $\Delta z/d$ when $\Delta x/d = 0.49$. The axial-force coefficient decreases rapidly with initial vertical displacement of the service module but tends to level out and then increase slightly when $\Delta z/d$ reaches 0.20. The initial decrease in C_A is not as pronounced as when $\Delta x/d = 0.20$ (fig. 17(a)) since the service module is further away the command module and its influence on C_A is somewhat reduced. The leveling out of C_A at large values of $\Delta x/d$ is expected since as $\Delta x/d$ approaches infinity this approximates the no-service-module case. The normal-force coefficient generally increases and the pitching-moment coefficient generally decreases with increasing $\Delta z/d$, particularly at high values of $\Delta z/d$.

The same trends of C_A , C_N , and C_m with increasing angle of attack and operation of the escape rocket are evident for $\Delta x/d = 0.49$ as they were for $\Delta x/d = 0.20$.

Effect of $\Delta \alpha_s$. - The effect of $\Delta \alpha_s$ on C_A , C_N , and C_m is shown in figure 18 for values of $\Delta z/d = 0$ and 0.20. Because an insufficient number of values of $\Delta \alpha_s$ were available, it was impossible to plot C_A , C_N , and C_m against $\Delta \alpha_s$. Therefore figure 18 shows C_A , C_N , and C_m plotted against angle of attack for the values of $\Delta \alpha_s$ tested. Figure 18(a) shows that increasing $\Delta \alpha_s$ decreases C_A except at $\alpha = 0^\circ$, where little or no effect is shown when $\Delta z/d = 0$. The shielding effect of the command module on the free-stream flow may account for this lack of change at $\alpha = 0^\circ$. When $\Delta z/d$ is increased to 0.20, an increase in $\Delta \alpha_s$ results in an increase of axial-force coefficient as shown in figure 18(b). This same trend was observed with increasing $\Delta x/d$ in figures 15(c) and 16 when the service module was initially displaced vertically ($\Delta z/d \neq 0$). Hence the effect of $\Delta \alpha_s$ on axial-force coefficient is dependent on the vertical displacement of the service module, as was the effect of $\Delta x/d$. The effect of $\Delta \alpha_s$ on C_A is smaller than the effect of $\Delta x/d$ or $\Delta z/d$ on C_A for all jet thrust coefficients tested. There is little or no effect of $\Delta \alpha_s$ on either C_N or C_m regardless of the value of $\Delta z/d$.

[REDACTED]

The effect of increasing $\Delta\alpha_s$ on C_A , C_N , and C_m is not greatly altered by changes in escape-rocket operation or angle of attack except at $\alpha = 0^\circ$, as previously noted, although the levels of C_A , C_N , and C_m are changed by both.

CONCLUSIONS

An investigation of a model of the Apollo launch-escape vehicle in close proximity to the service module and including the effects of escape-rocket-exhaust interference has been conducted. The results of the investigation have led to the following conclusions:

1. The small initial longitudinal displacement between the service module and command module during separation produces a very pronounced decrease in base pressures and a large increase in axial force (drag) on the launch-escape vehicle.

2. The pressures on the conical surface of the command module are not affected by the service module except slightly when the service module is displaced vertically.

3. In general, although angle of attack and escape-rocket operation affect the levels of axial-force, normal-force, and pitching-moment coefficients, the effect of increasing one of the three service-module displacement parameters on these coefficients was not greatly altered by either angle of attack or escape-rocket operation.

4. The effect of longitudinal displacement of the service module on the aerodynamic characteristics of the launch-escape vehicle is dependent to a large degree on the vertical displacement of the service module and to a smaller degree on the relative angle of attack between the command module and service module. In general, the axial-force coefficient decreases with increasing longitudinal displacement of the service module, when the service module is not displaced vertically, regardless of the relative angle of attack between the command module and service module. When the service module is displaced vertically, any increase in the longitudinal displacement of the service module generally increases the axial-force coefficient and, depending on the value of the relative angle of attack between the command module and service module, may reach a maximum value and then decrease. Normal-force coefficient and pitching-moment coefficient are not affected by increasing the longitudinal displacement of the service module except when the service module is displaced vertically.

5. The base pressures generally tend to approach the values obtained for the no-service-module case as longitudinal displacement of the service module increases.

6. The base pressures are increased and the axial-force coefficient is decreased with increasing vertical displacement of the service module, regardless of the value of the other displacement parameters of the service module.

[REDACTED]

Normal-force coefficient generally increases and pitching-moment coefficient generally decreases with increasing vertical displacement of the service module.

7. The effect of relative angle of attack between the command module and service module on the base pressures of the command module and the axial-force coefficient of the launch-escape vehicle is dependent upon the values of the other two service module displacement parameters and angle of attack. Relative angle of attack between the command module and service module had little or no effect on normal-force coefficient or pitching-moment coefficient of the launch-escape vehicle. The effect of relative angle of attack between the command module and service module is generally less than the effect of either longitudinal or vertical displacement of the service module on the launch-escape vehicle.

Langley Research Center,
National Aeronautics and Space Administration,
Langley Station, Hampton, Va., October 3, 1966,
124-07-02-02-23.

REFERENCES

1. Babcock, D. L.; and Wiltse, P. D.: Motor-Vehicle Interfaces in the Apollo Launch Escape System. Paper No. 65-152, Am. Inst. Aeron. Astronaut., Feb. 1965.
2. Runckel, Jack F.; Schmeer, James W.; and Pendergraft, Odis C., Jr.: Static Longitudinal Aerodynamic Characteristics of a Powered Model of the Apollo Launch-Escape Vehicle From Mach 0.50 to 1.30. NASA TM X-1215, 1966.
3. Runckel, Jack F.; and Swihart, John M.: A Hydrogen Peroxide Hot-Jet Simulator for Wind-Tunnel Tests of Turbojet-Exit Models. NASA MEMO 1-10-59L, 1959.
4. Cahn, Maurice S.: An Experimental Investigation of Sting-Support Effects on Drag and a Comparison With Jet Effects at Transonic Speeds. NACA Rept. 1353, 1958. (Supersedes NACA RM L56F18a.)

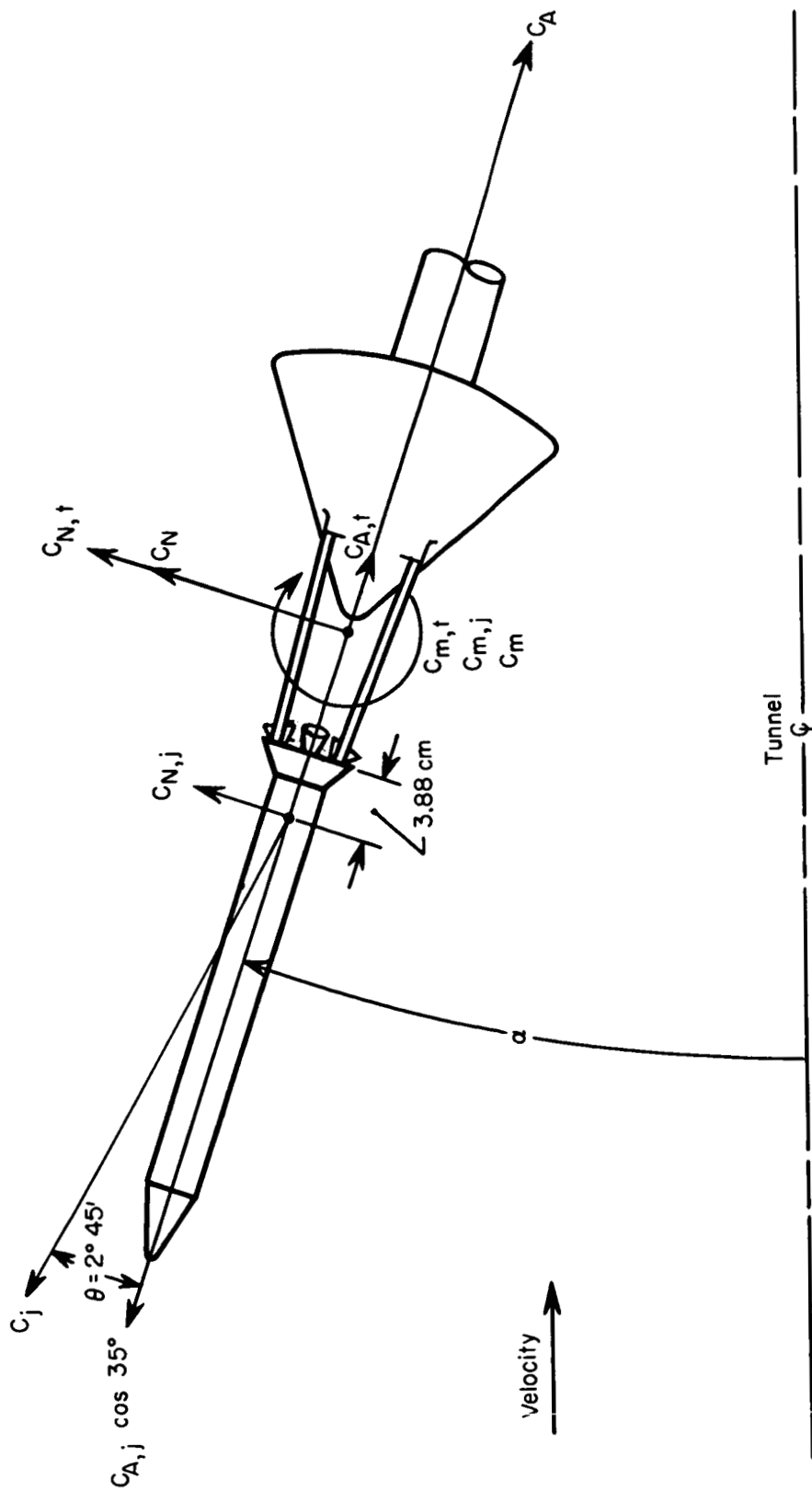
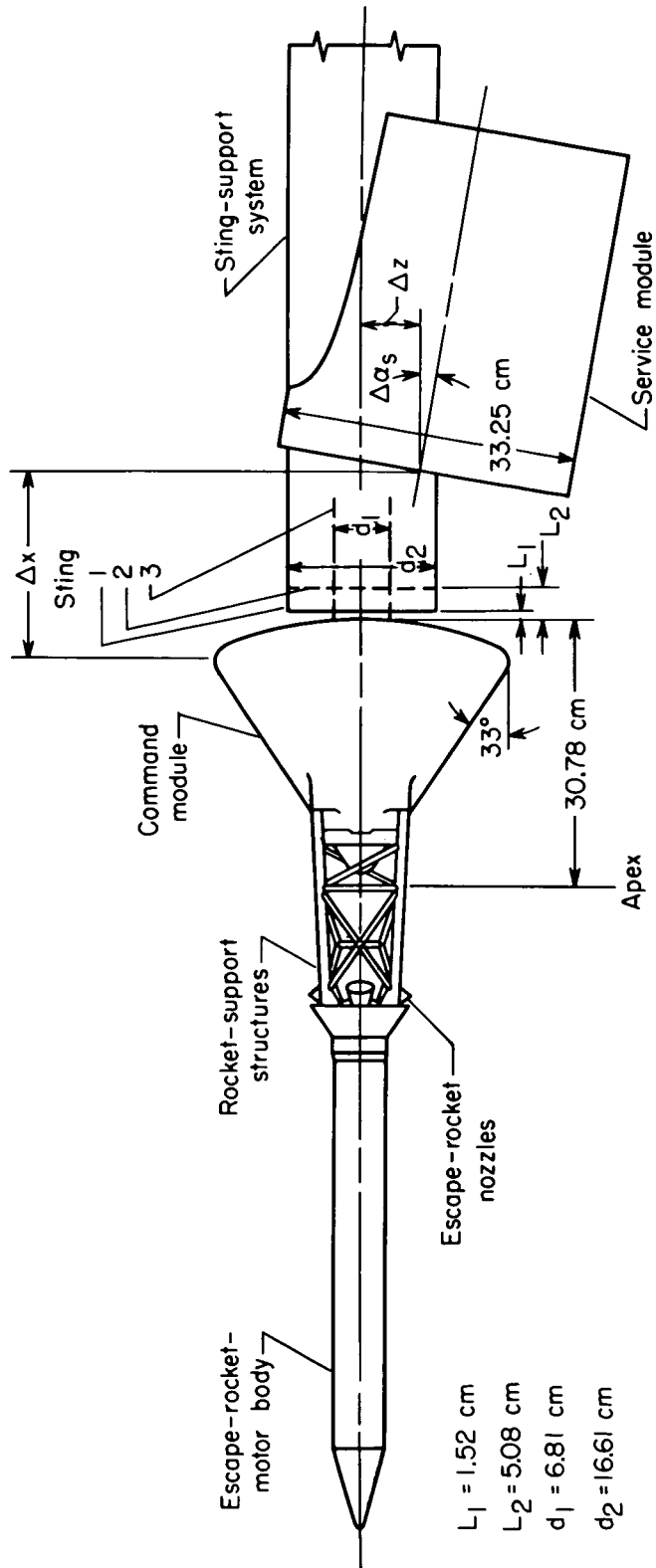
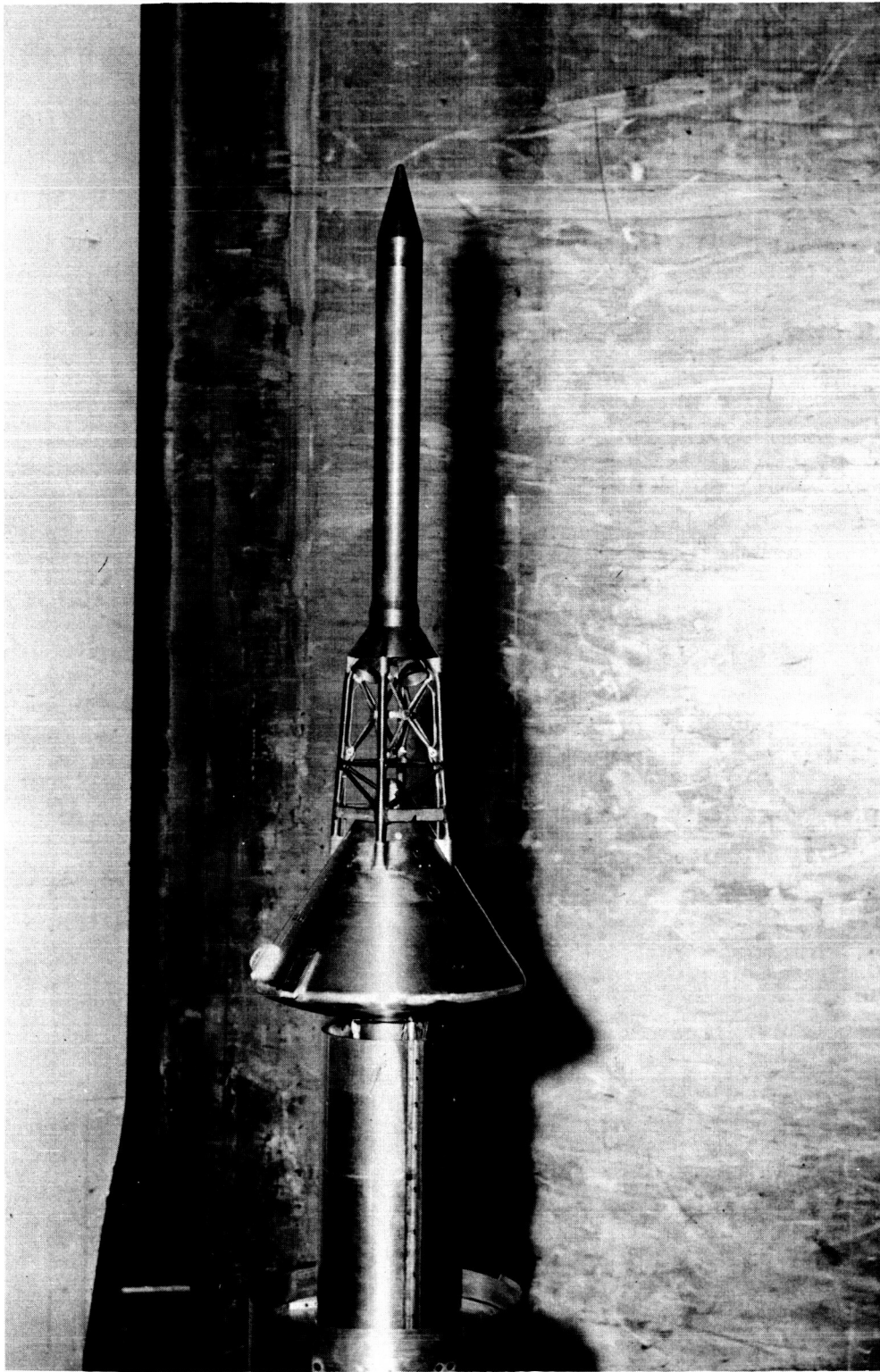


Figure 1.- Body system of axes. Force and moment coefficients on model including rocket thrust components. Arrows indicate positive direction.

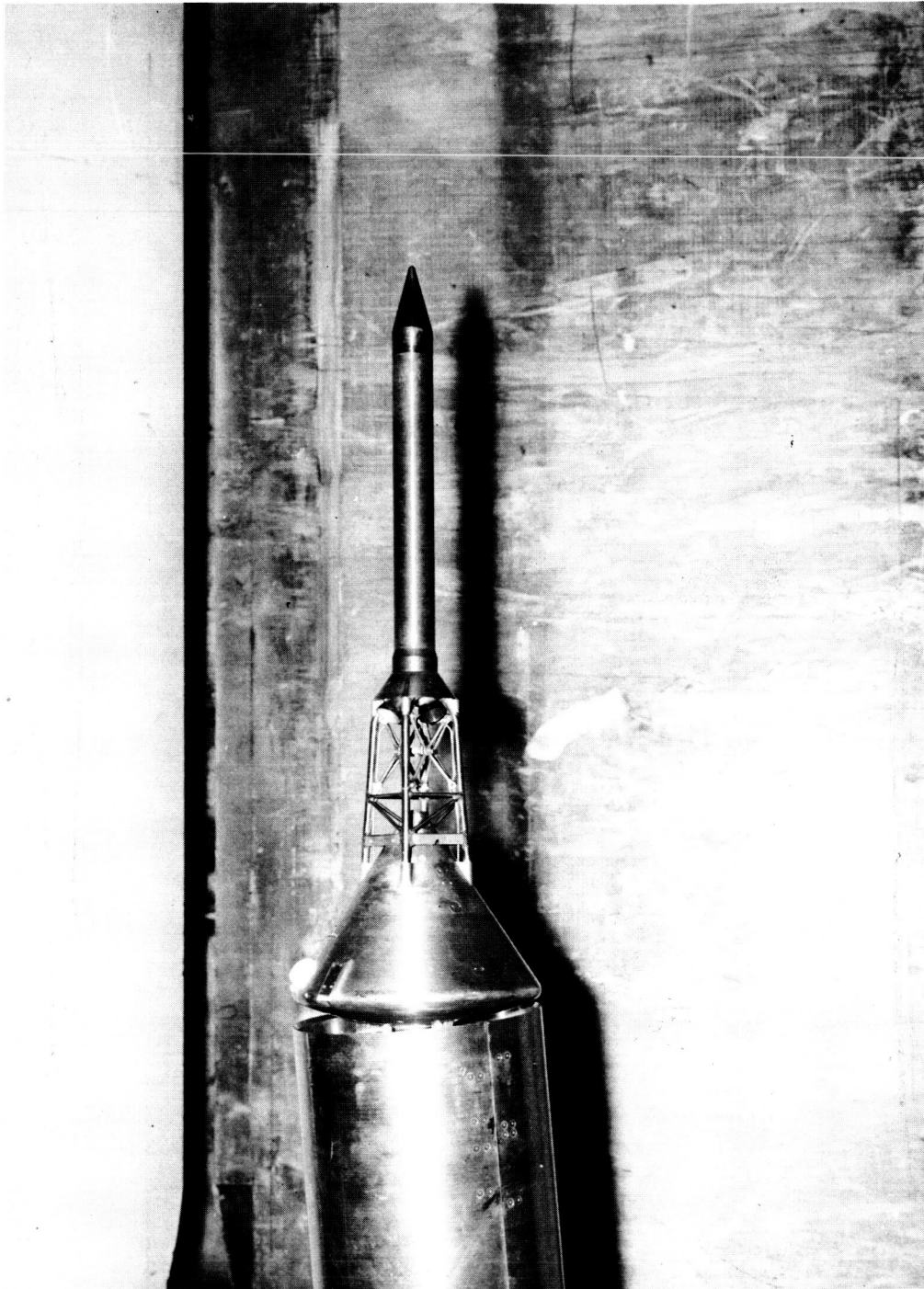


| List of configurations | | | | | | | | | |
|------------------------|-------|--------------|-------------------------|---------------------------------|---------------|-------|--------------|-------------------------|-----------------------|
| Configuration | Sting | $\Delta z/d$ | $\Delta \alpha_s$, deg | Range of $\Delta x/d$ | Configuration | Sting | $\Delta z/d$ | $\Delta \alpha_s$, deg | Range of $\Delta x/d$ |
| 1 | 1 | 0 | 0 | 0.01, 0.20, 0.49, 1.30 | 7 | 1 | 0.1 | 10 | 0.20, 0.49, 1.30 |
| 1 | 2 | 0 | 0 | 0.013, 0.039, 0.136, 0.25, 0.50 | 8 | 1 | .2 | 10 | 0.20 |
| 2 | 1 | .1 | 0 | 0.10, 0.20, 0.49, 1.30 | 9 | 1 | .2 | 20 | 0.20, 0.49, 1.3 |
| 3 | 1 | .2 | 0 | 0.20, 0.49, 1.30 | 10 | 1 | .5 | 20 | 0.20, 0.49, 1.14 |
| 4 | 1 | .5 | 0 | 0.49 | 11 | 1 | | | |
| 5 | 1 | 0 | 5 | 0.10, 0.20, 0.49, 1.30 | 12 | 3 | | No service module | |
| 6 | 1 | 0 | 10 | 0.20, 0.49, 1.30 | | | | | |

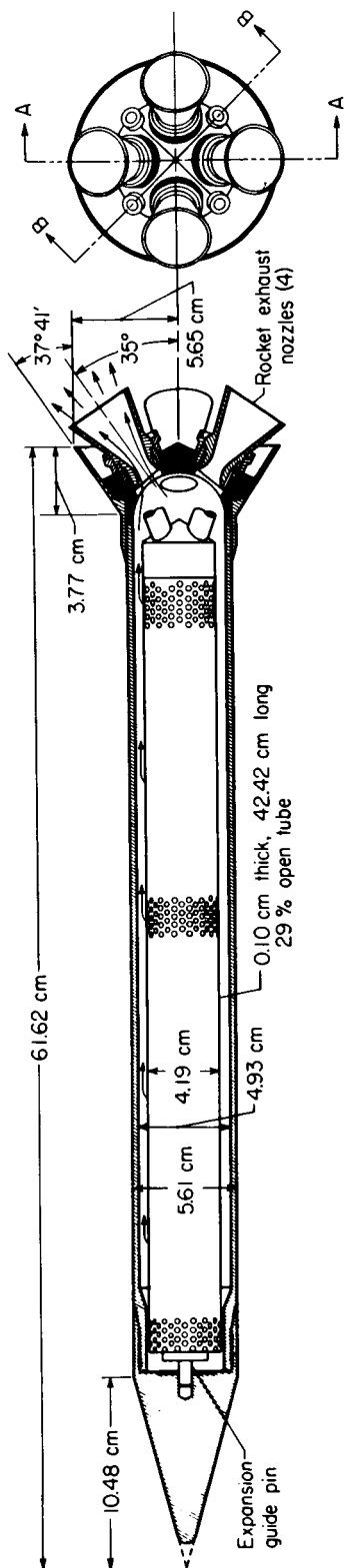
Figure 2.- Sketch of Apollo launch-escape vehicle with service module.



L-64-2458
Figure 3.- Photograph of Apollo launch-escape vehicle with service module; configuration 1; $\Delta z/d = 0$; $\Delta x/d = 1.3$; $\Delta \alpha_S = 0^\circ$.



L-64-2568
Figure 4.- Photograph of Apollo launch-escape vehicle with service module; configuration 5; $\Delta z/d = 0$; $\Delta x/d = 0.1$; $\Delta \alpha_s = 5^\circ$.



Section A-A
Gas Flow Passage

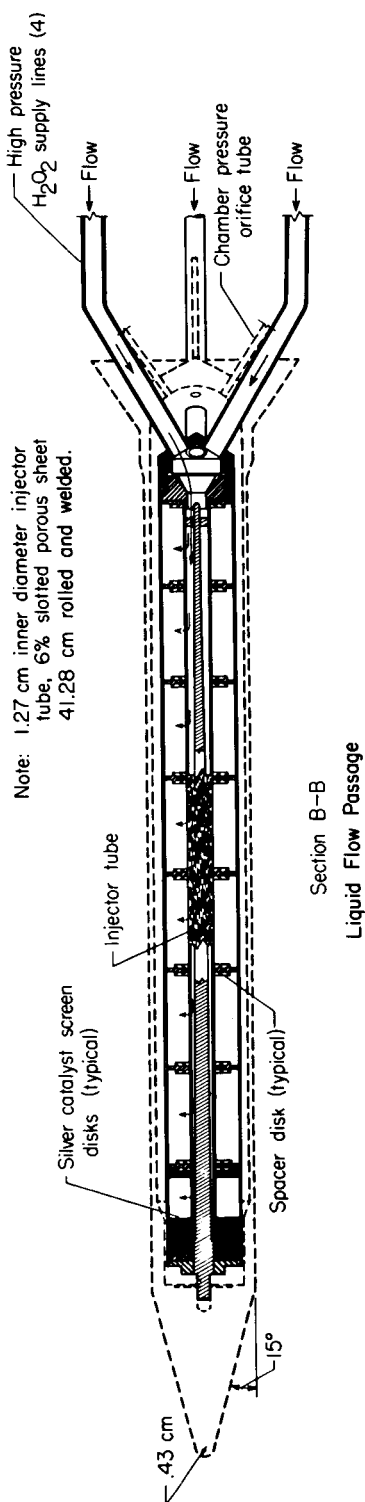
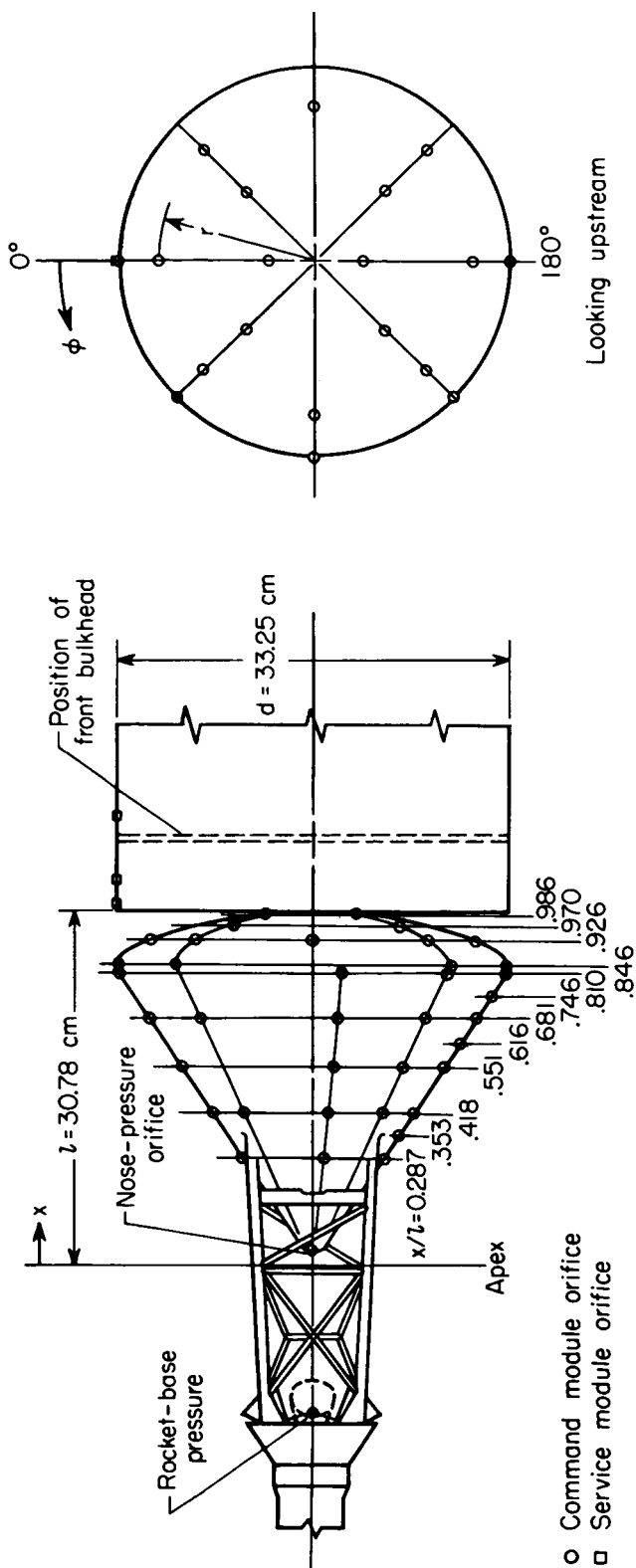
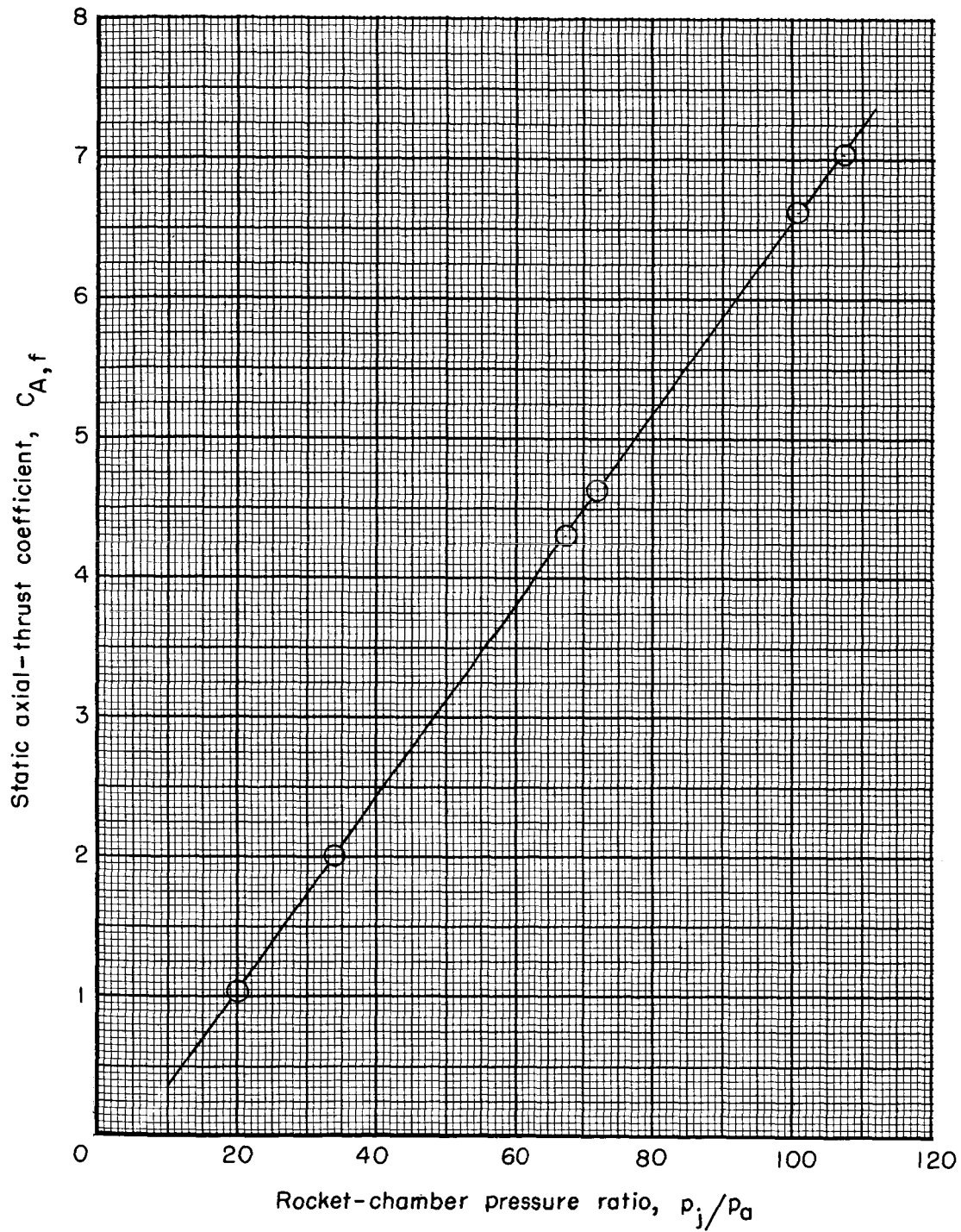


Figure 5.- Sketch of rocket decomposition chamber.



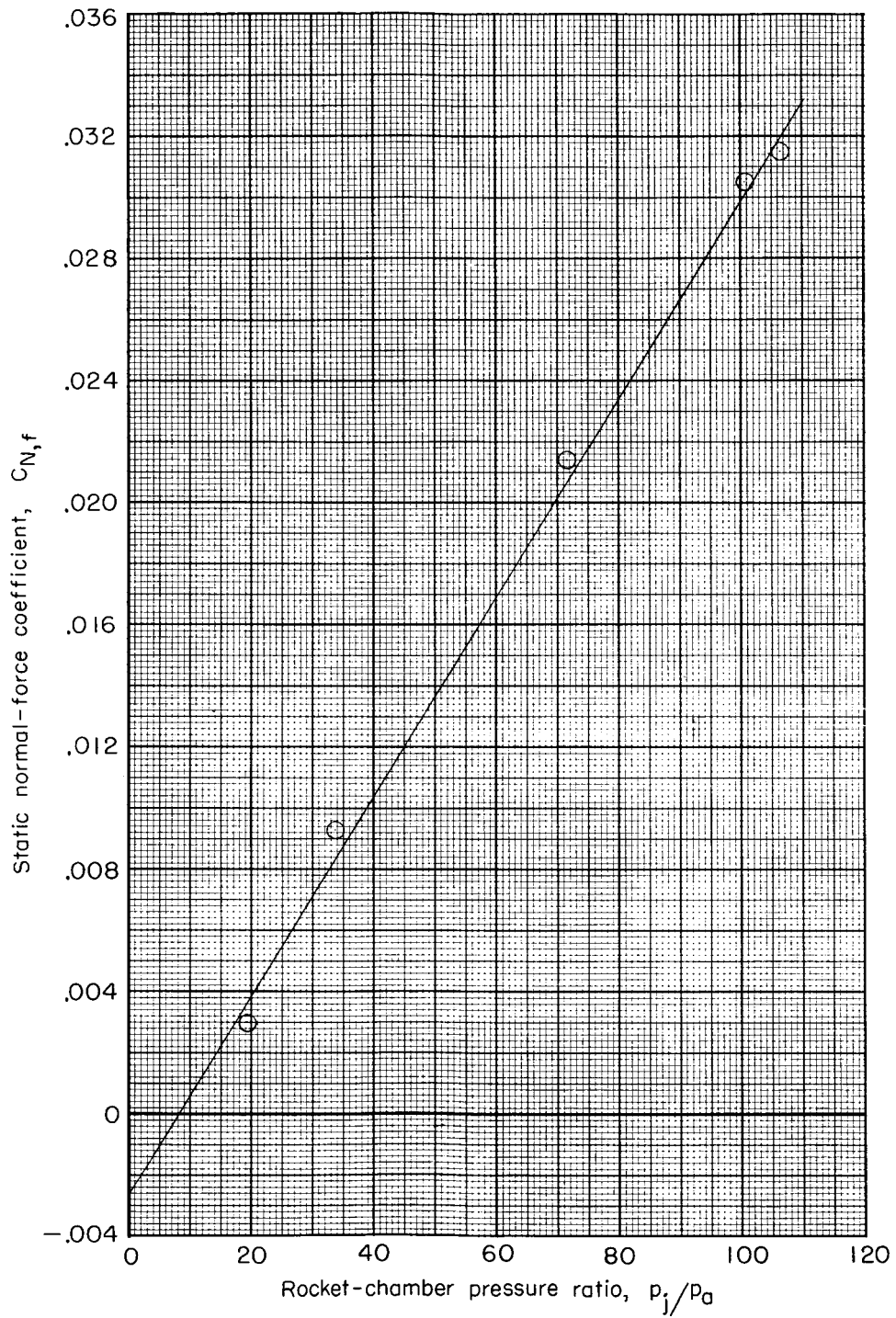
| x/l | ϕ , deg | Remarks | r/d | x/l | ϕ , deg | Remarks | r/d |
|--------|-----------------------|----------------------|-------|-------|------------------------------------|---|-------|
| -.0351 | | Rocket base | | 0.810 | 0, 97.5, 135, 180 | Conical surface | |
| .054 | | Conical surface nose | | .846 | 0, 45, 135, 180 | Conical surface (max. diam.) | .50 |
| .287 | 0, 97.5, 180 | Conical surface | | .926 | 0, 45, 90, 135, 180, 225, 270, 315 | Base | .40 |
| .353 | 180 | Conical surface | | .970 | 45, 135, 225, 315 | Base | .25 |
| .418 | 0, 45, 97.5, 135, 180 | Conical surface | | .986 | 0, 180 | Base | .12 |
| .551 | 0, 97.5, 135, 180 | Conical surface | | 1.022 | 0 | Service module surface ($\Delta x/d=0$) | .50 |
| .616 | 180 | Conical surface | | 1.086 | 0 | Service module surface ($\Delta x/d=0$) | .50 |
| .681 | 0, 45, 97.5, 135, 180 | Conical surface | | 1.259 | 0 | Service module surface ($\Delta x/d=0$) | .50 |
| .746 | 180 | Conical surface | | | | | |

Figure 6.- Sketch showing pressure-orifice locations on model.



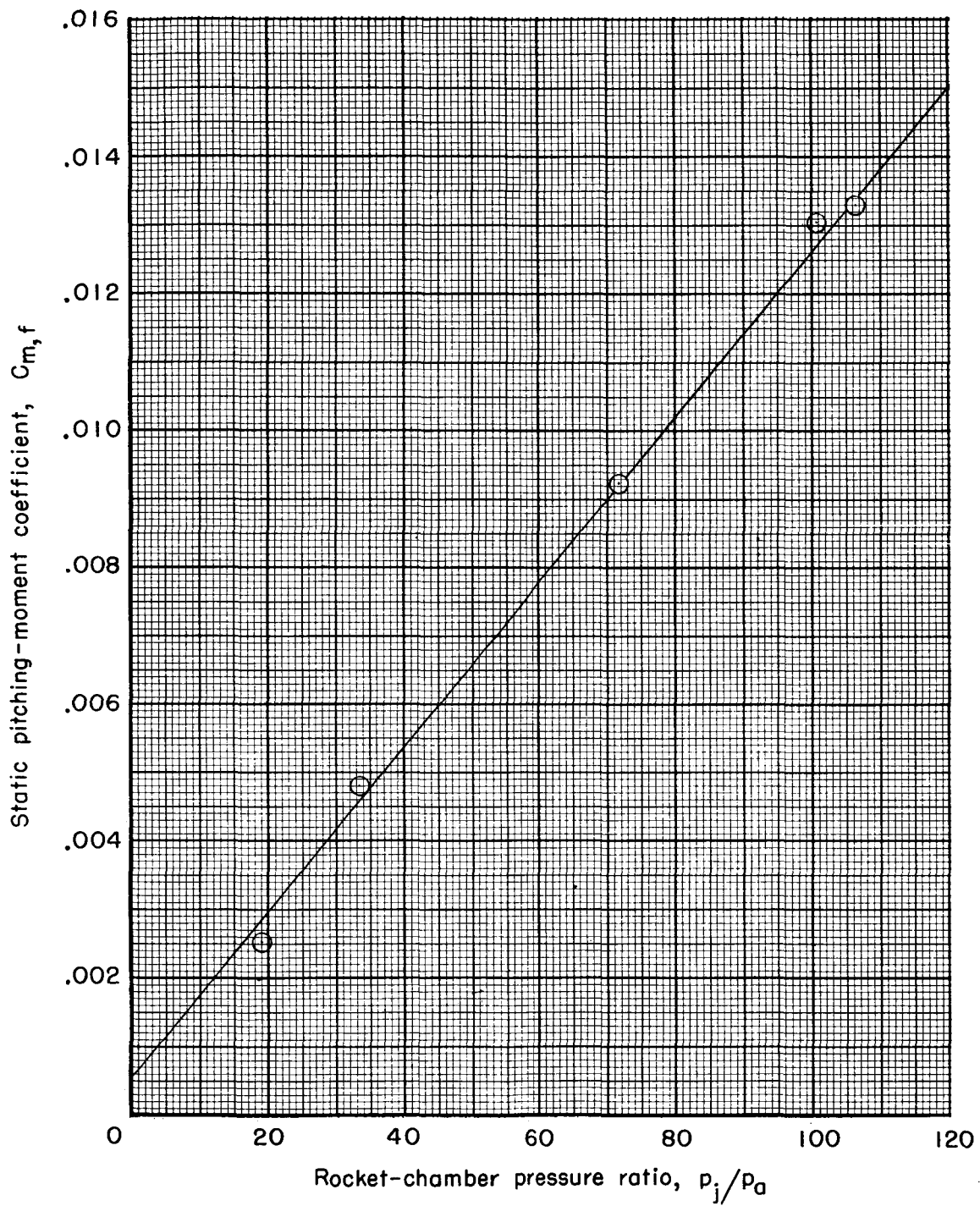
(a) Variation of axial-force coefficient with rocket-chamber pressure ratio.

Figure 7.- Static thrust calibrations of launch-escape vehicle.



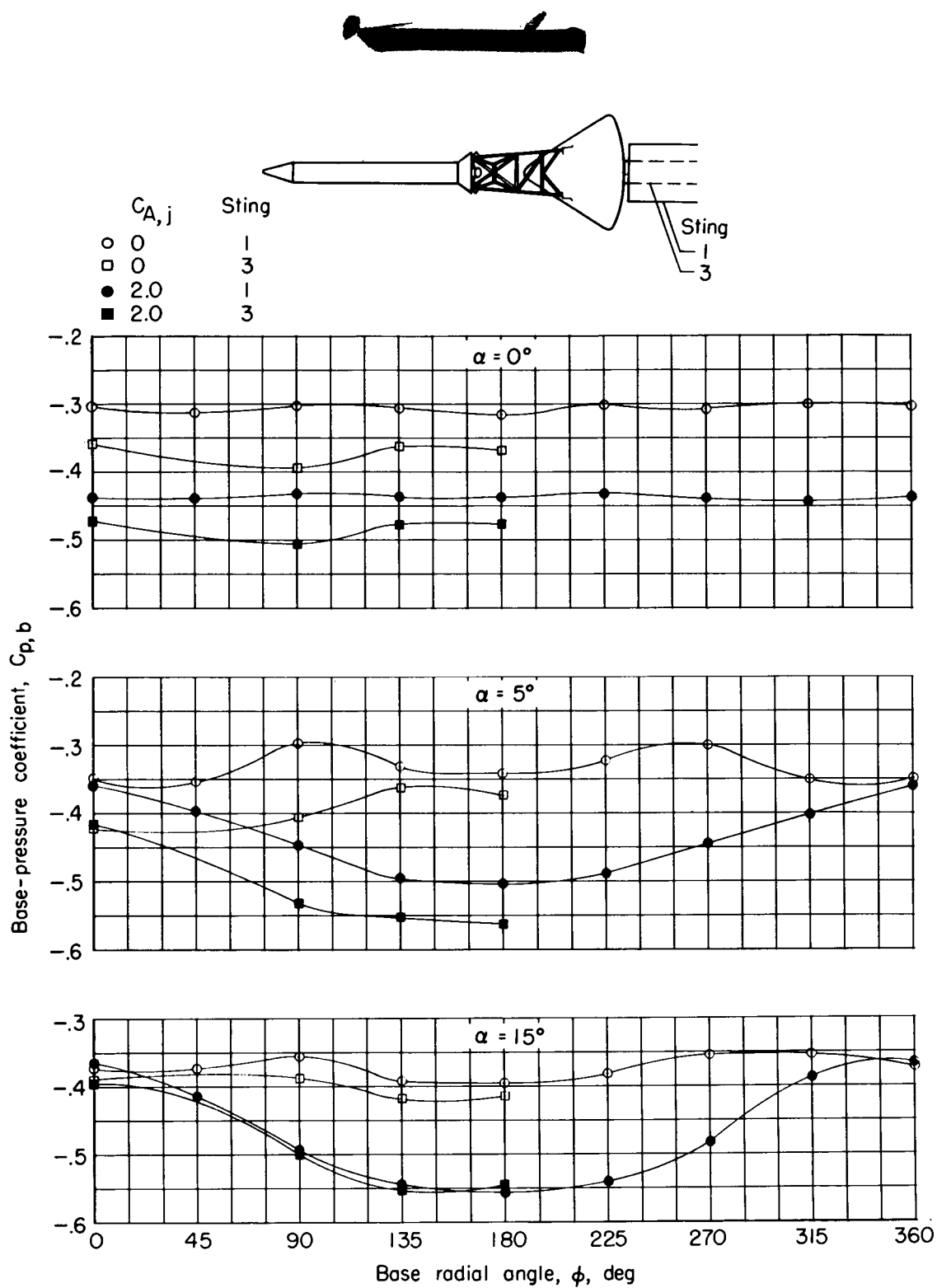
(b) Variation of normal-force coefficient with rocket-chamber pressure ratio.

Figure 7.- Continued.



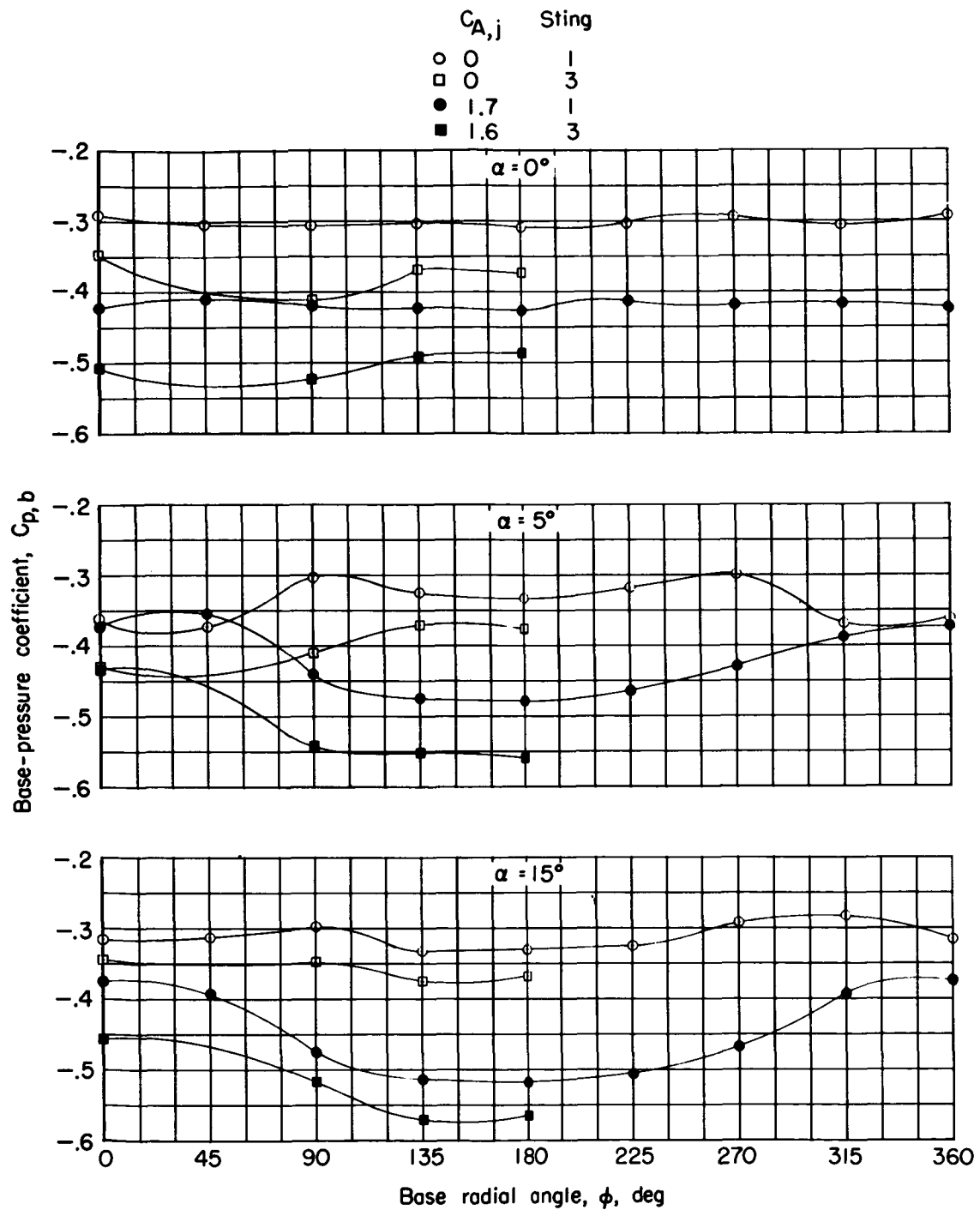
(c) Variation of pitching-moment coefficient about apex with rocket-chamber pressure ratio.

Figure 7.- Concluded.



(a) $M = 0.90$.

Figure 8.- Effect of sting interference on command-module base-pressure coefficients; no service module; $r/d = 0.40$.



(b) $M = 1.10$.

Figure 8.- Concluded.

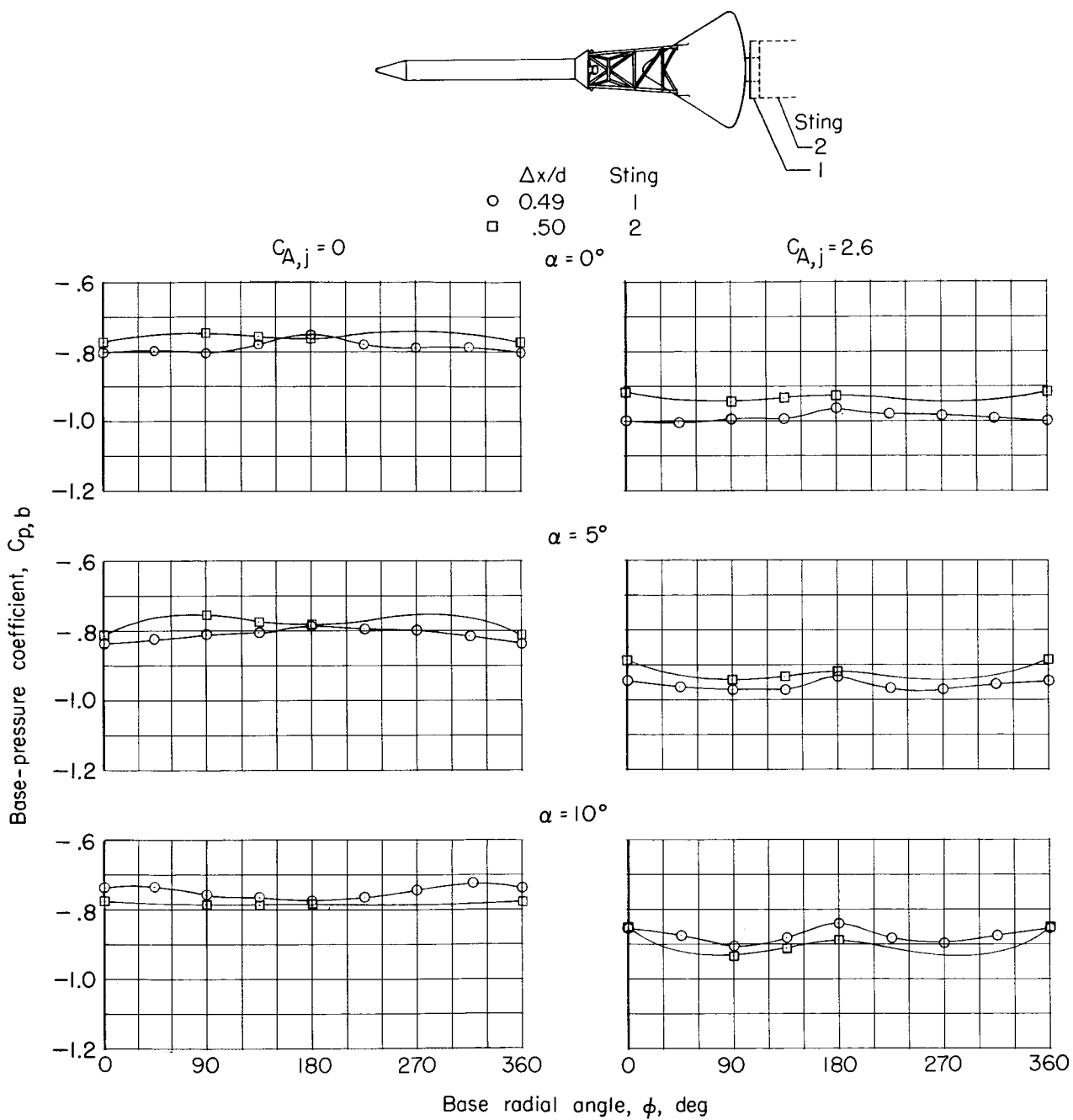
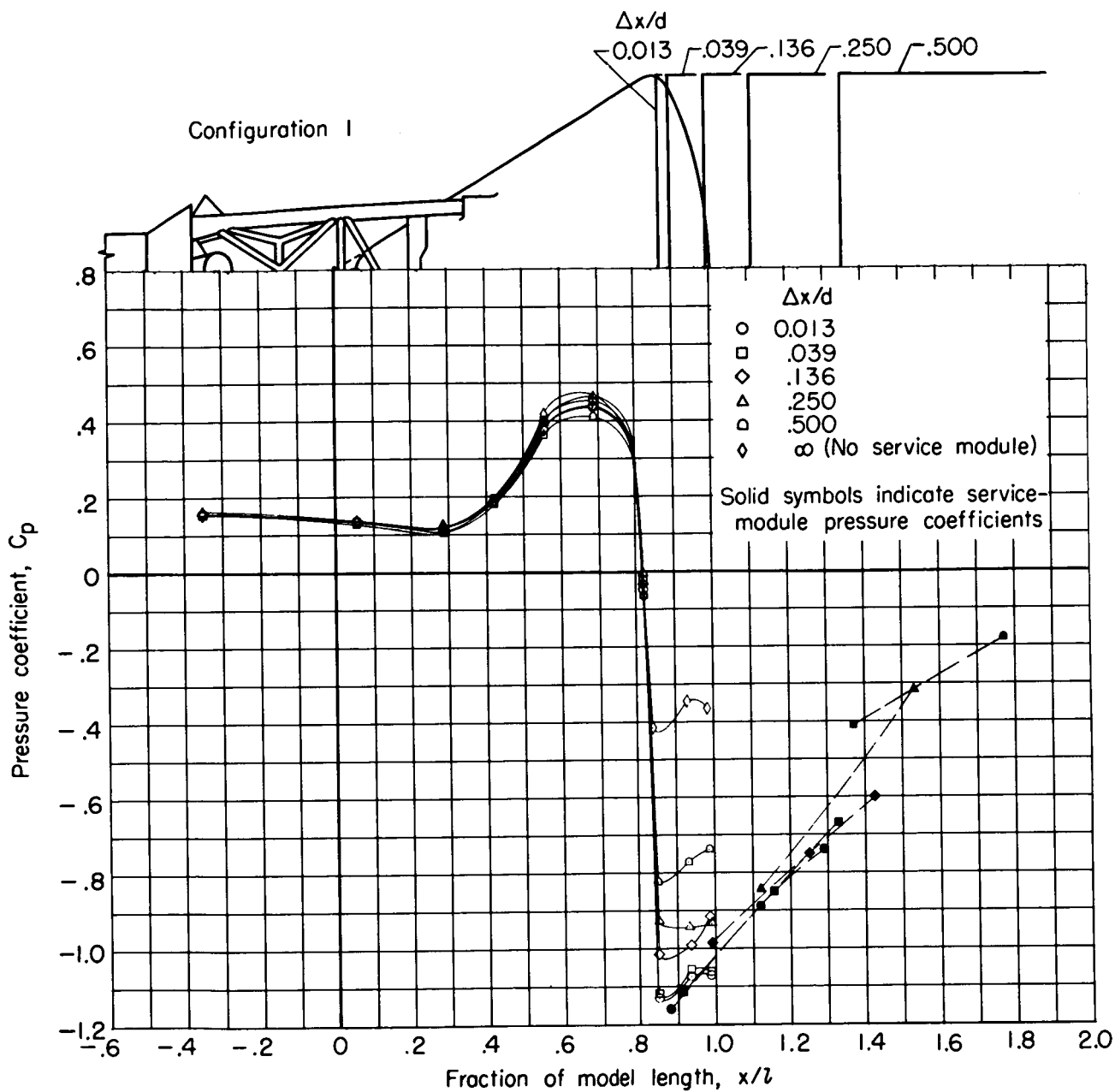
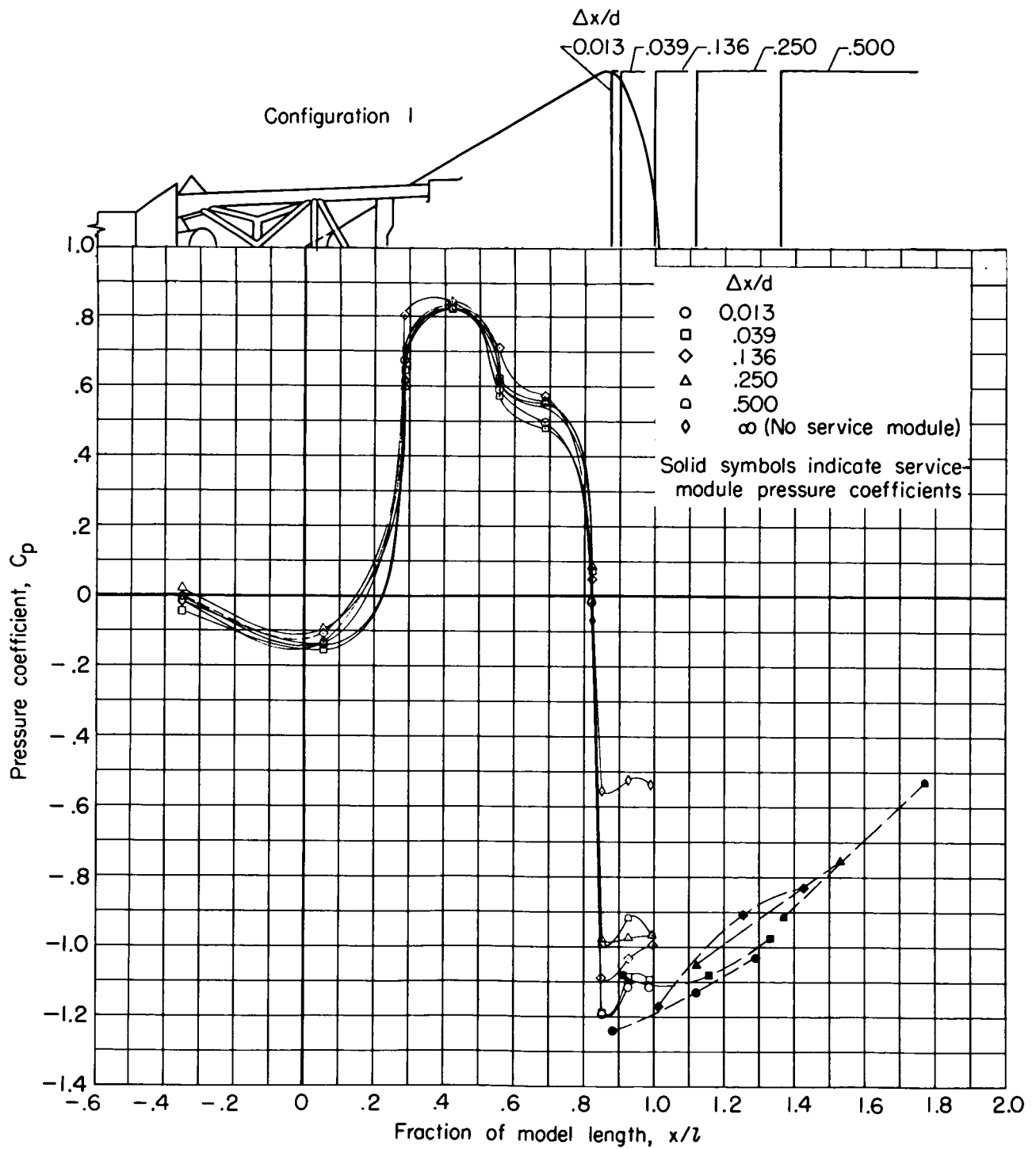


Figure 9.- Effect of sting interference on command-module base-pressure coefficients; $M = 0.90$; $\Delta z/d = 0$; $\Delta \alpha_s = 0^\circ$; $r/d = 0.40$.



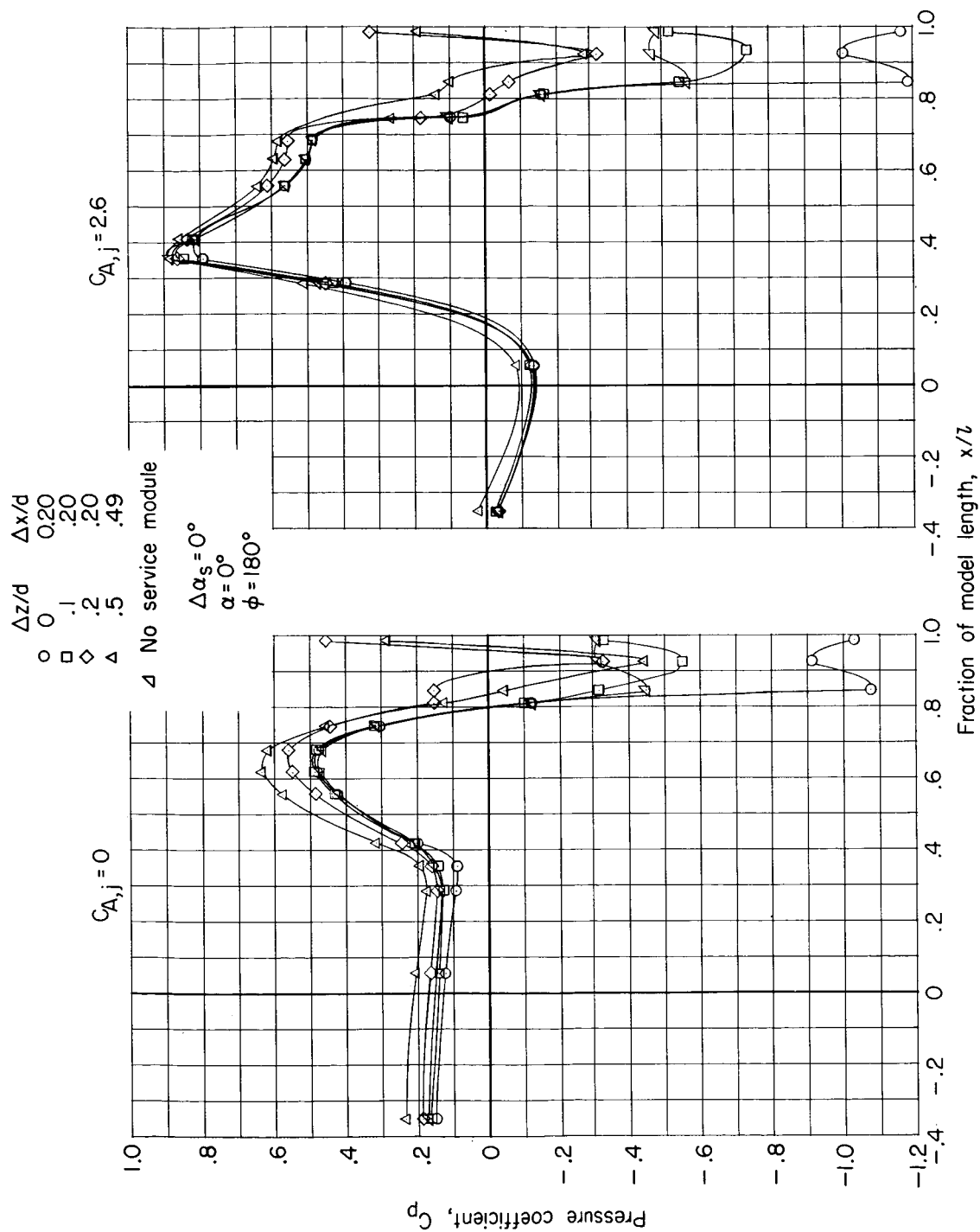
(a) $C_{A,j} = 0$.

Figure 10.- Pressure distributions on launch-escape vehicle and service module for variable $\Delta x/d$; $M = 0.90$; $\alpha = 0^\circ$; $\Delta z/d = 0$; $\Delta \alpha_s = 0^\circ$; $\phi = 0^\circ$; sting 2.



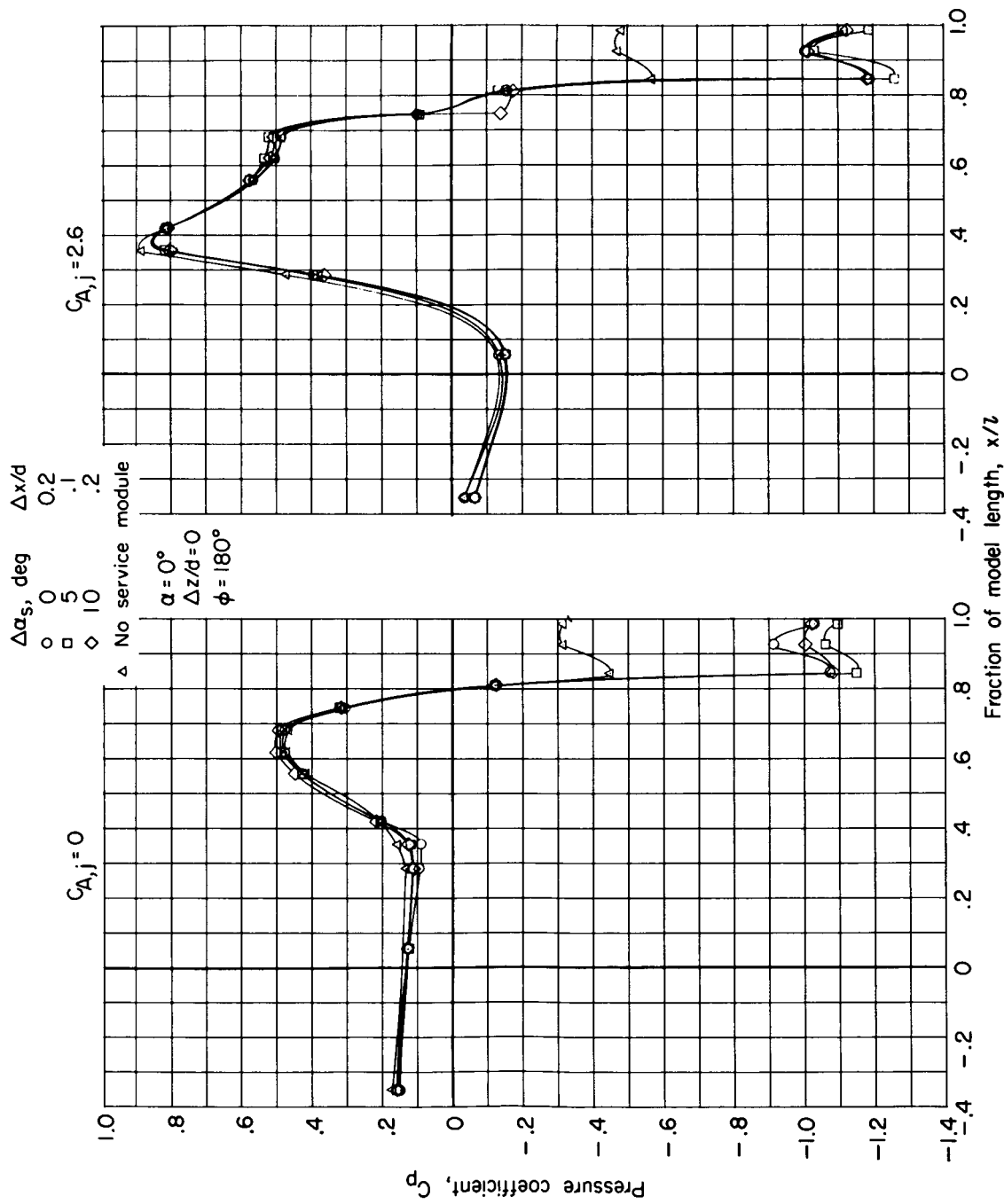
(b) $C_{A,j} = 2.5$.

Figure 10.- Concluded.



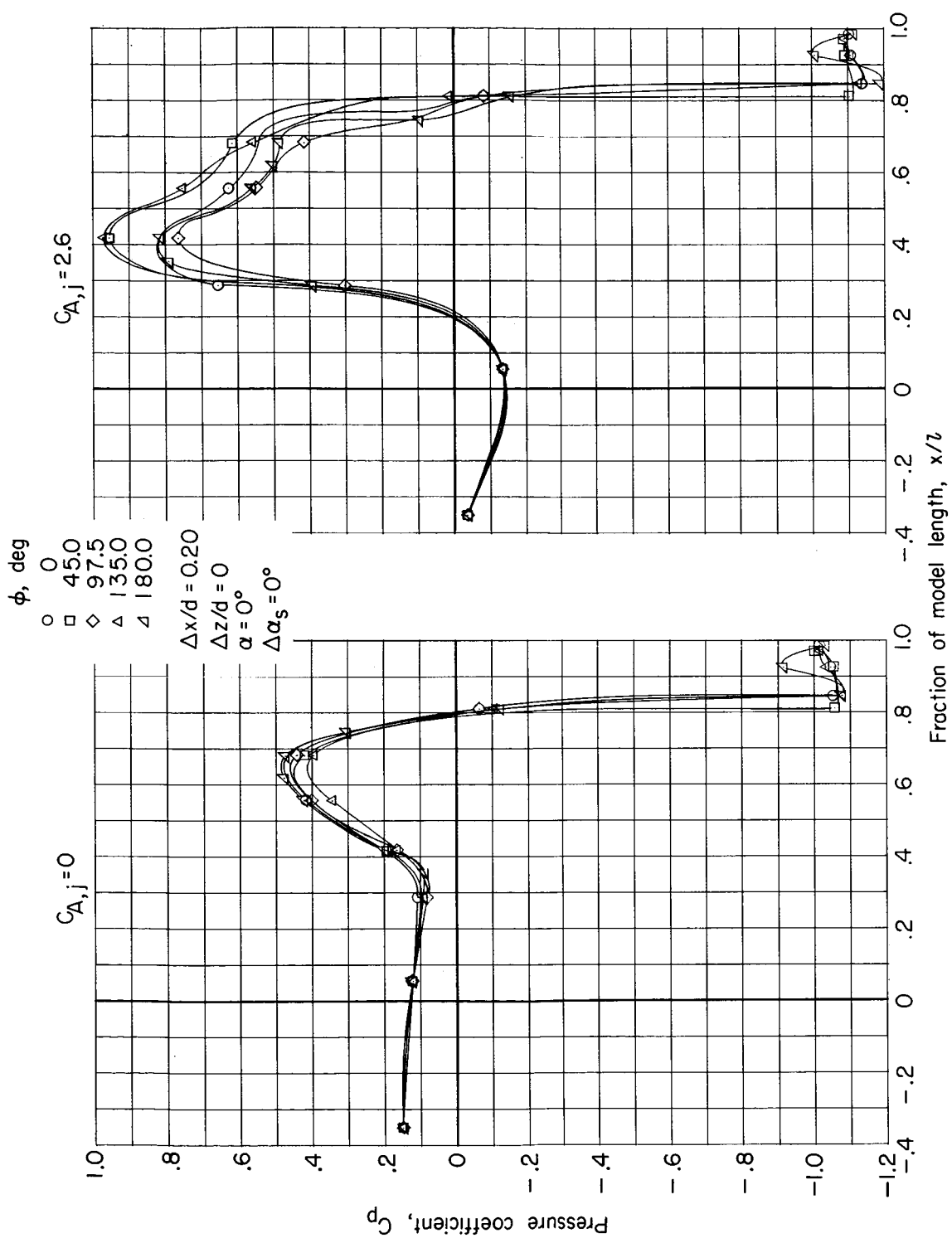
(a) Variable $\Delta z/d$.

Figure 11.- Pressure distributions on launch-escape vehicle; $M = 0.90$.



(b) Variable $\Delta\alpha_s$.

Figure 11.- Continued.



(c) Variation of ϕ .

Figure 11.- Continued.

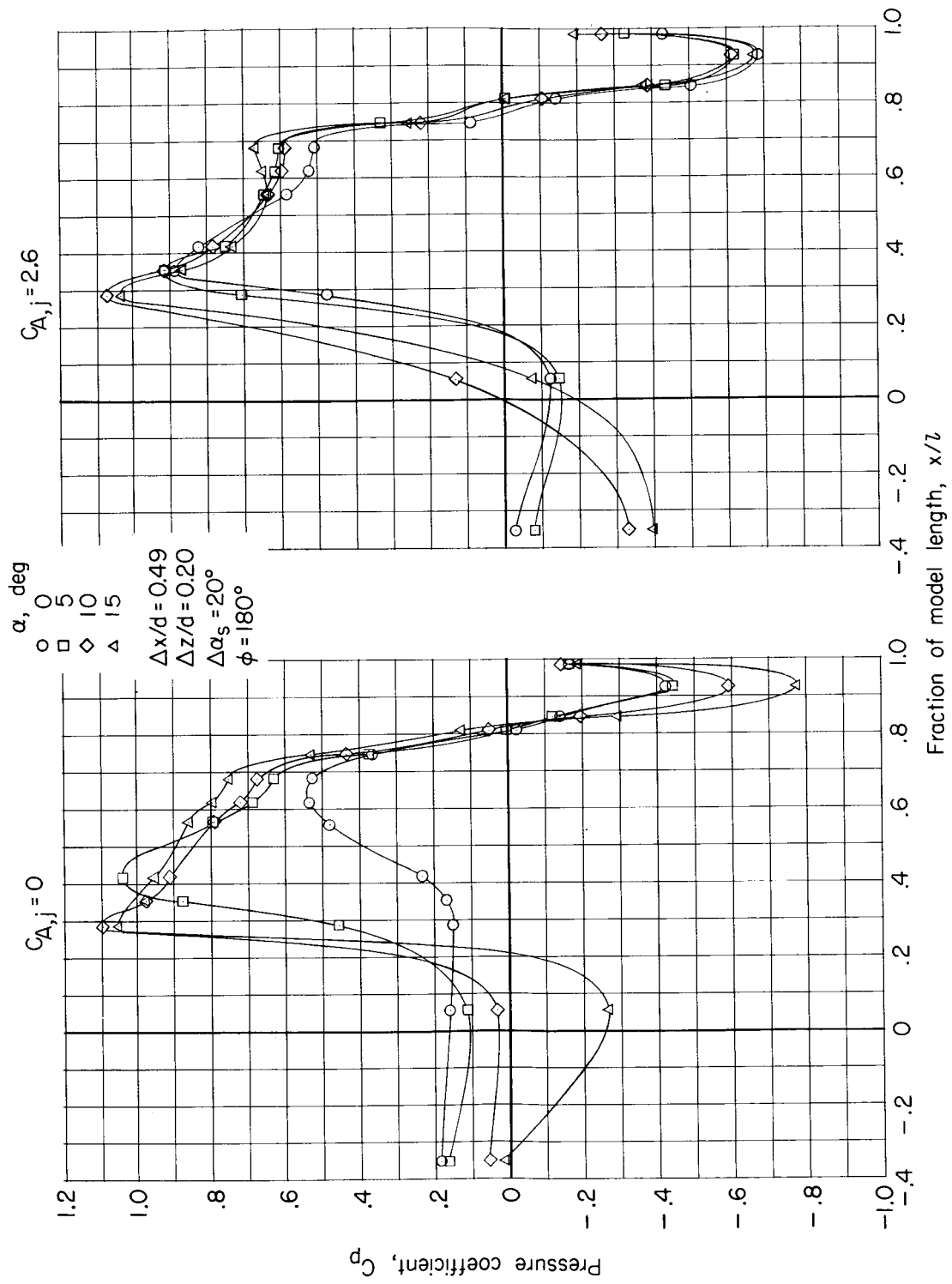
(d) Variable α .

Figure 11.- Concluded.

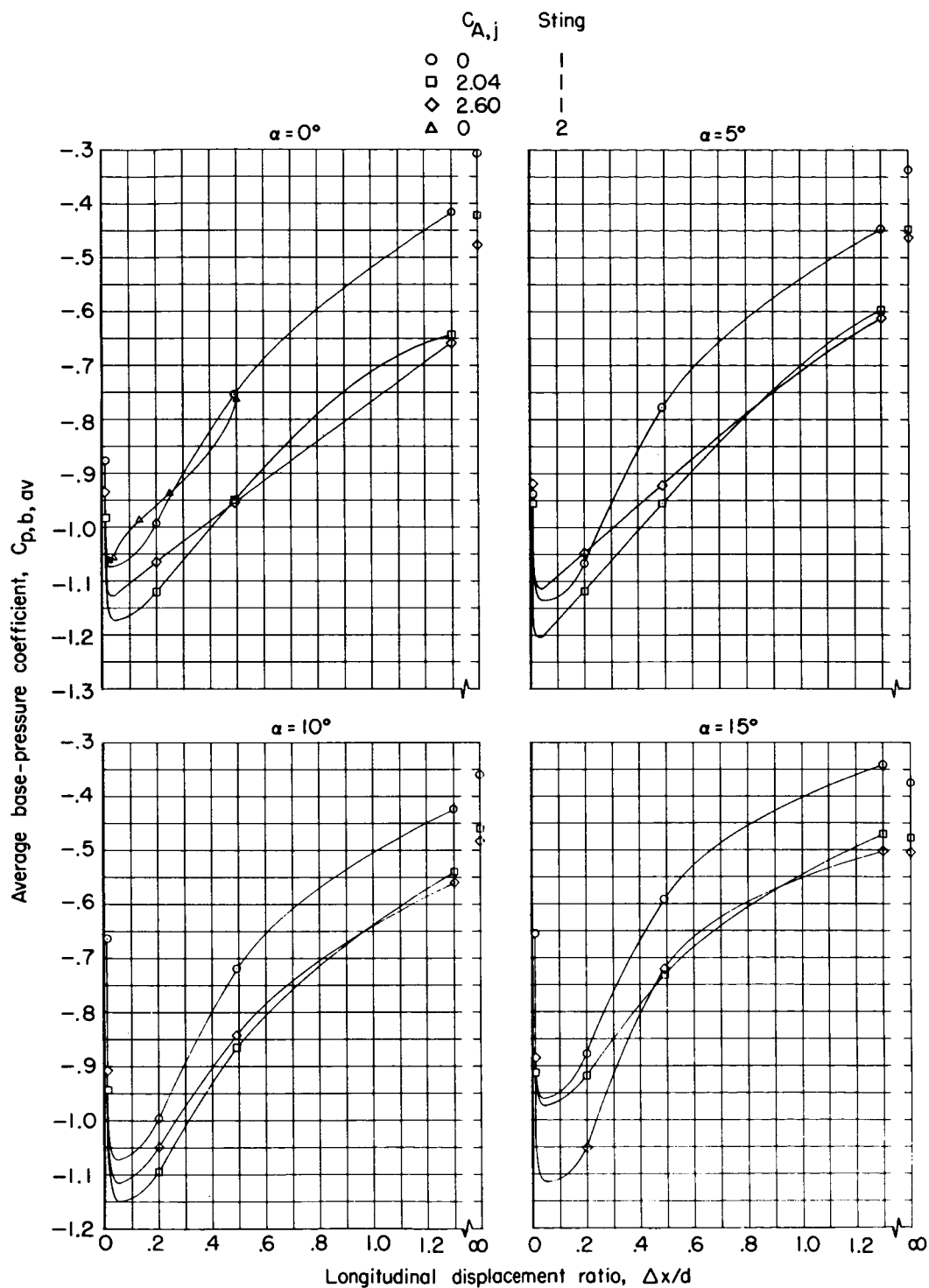


Figure 12.- Effect of longitudinal displacement of service module on average base-pressure coefficients of command module; $M = 0.90$; $\Delta z/d = 0$; $\Delta \alpha_s = 0^\circ$. Isolated symbols indicate no service module.

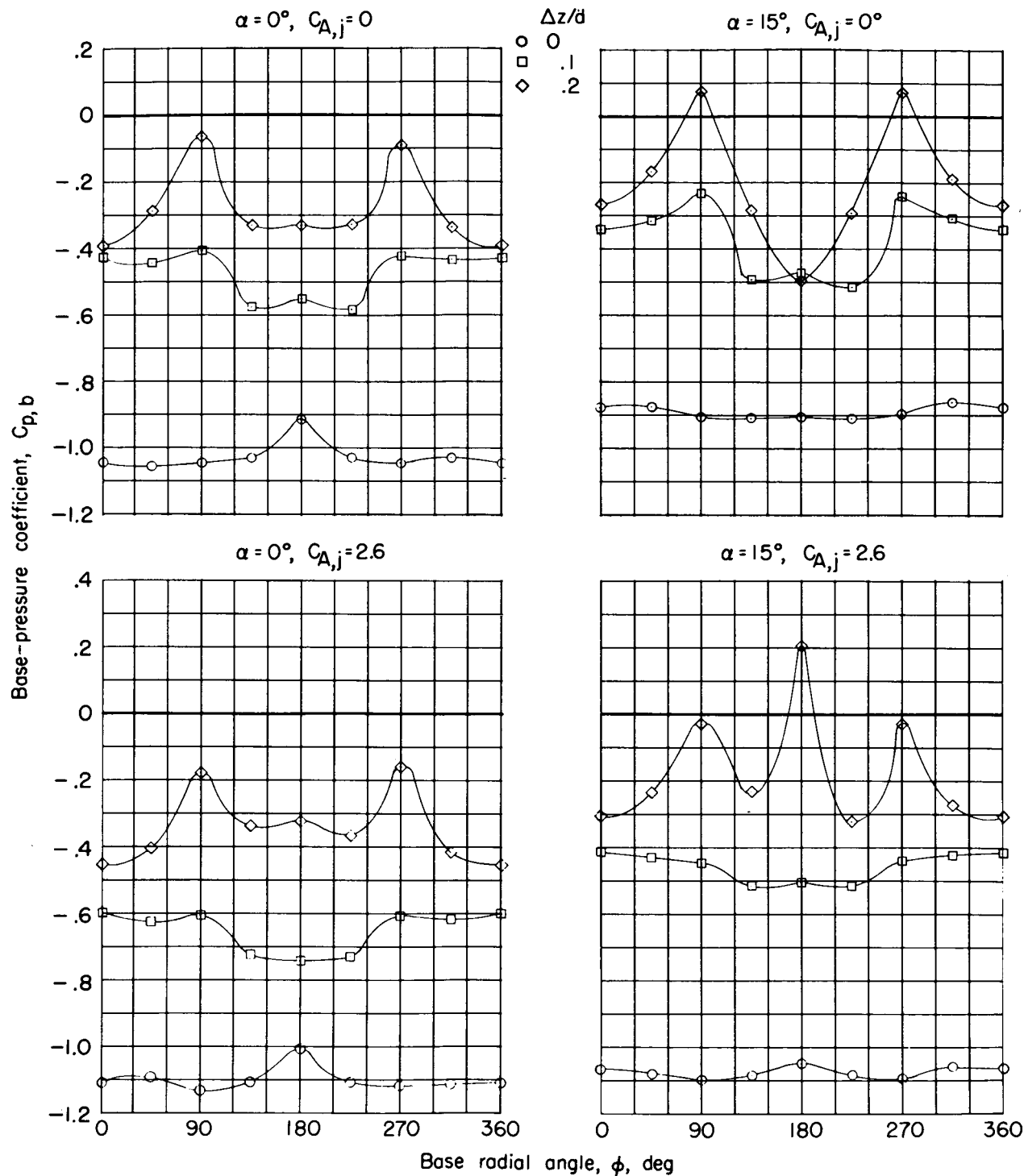
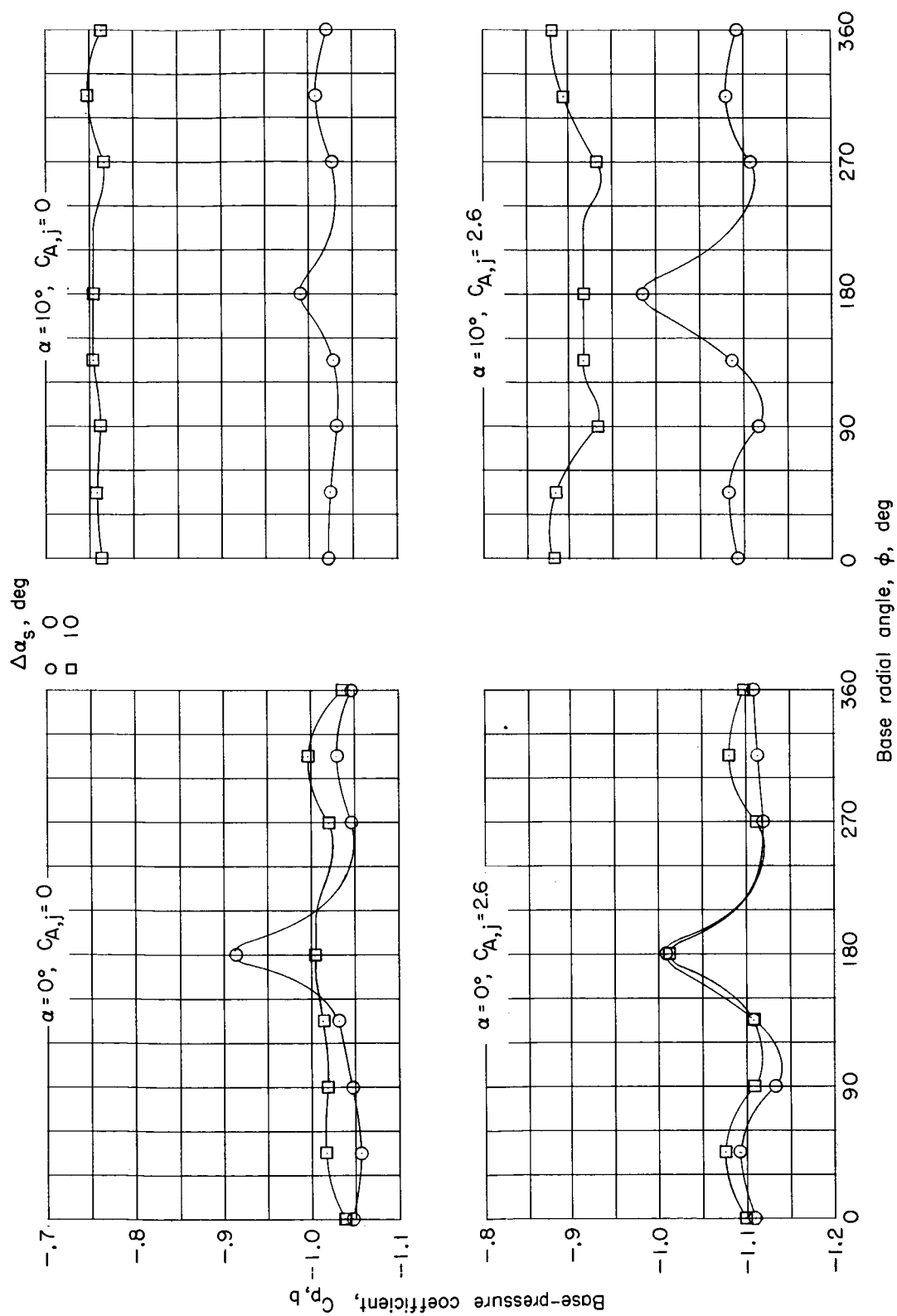
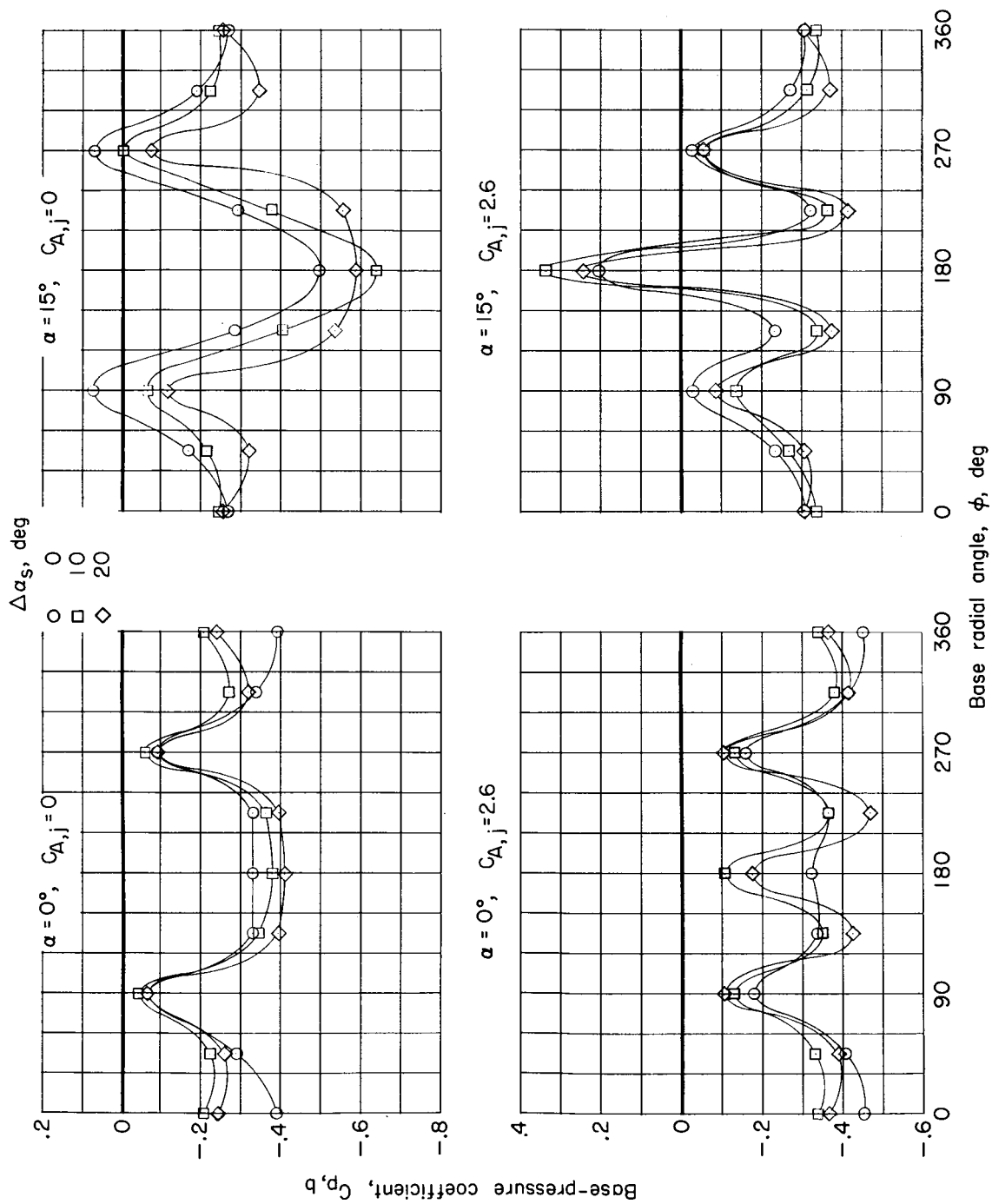


Figure 13.- Effect of vertical displacement of service module on command-module base-pressure coefficients; $M = 0.90$; $\Delta x/d = 0.20$; $\Delta \alpha_s = 0^\circ$; $r/d = 0.40$.



(a) $\Delta z/d = 0$.

Figure 14.- Effect of $\Delta\alpha_s$ on base pressures at various radial angles; $M = 0.90$; $\Delta x/d = 0.20$; $r/d = 0.40$.



(b) $\Delta z/d = 0.2$.

Figure 14.- Concluded.

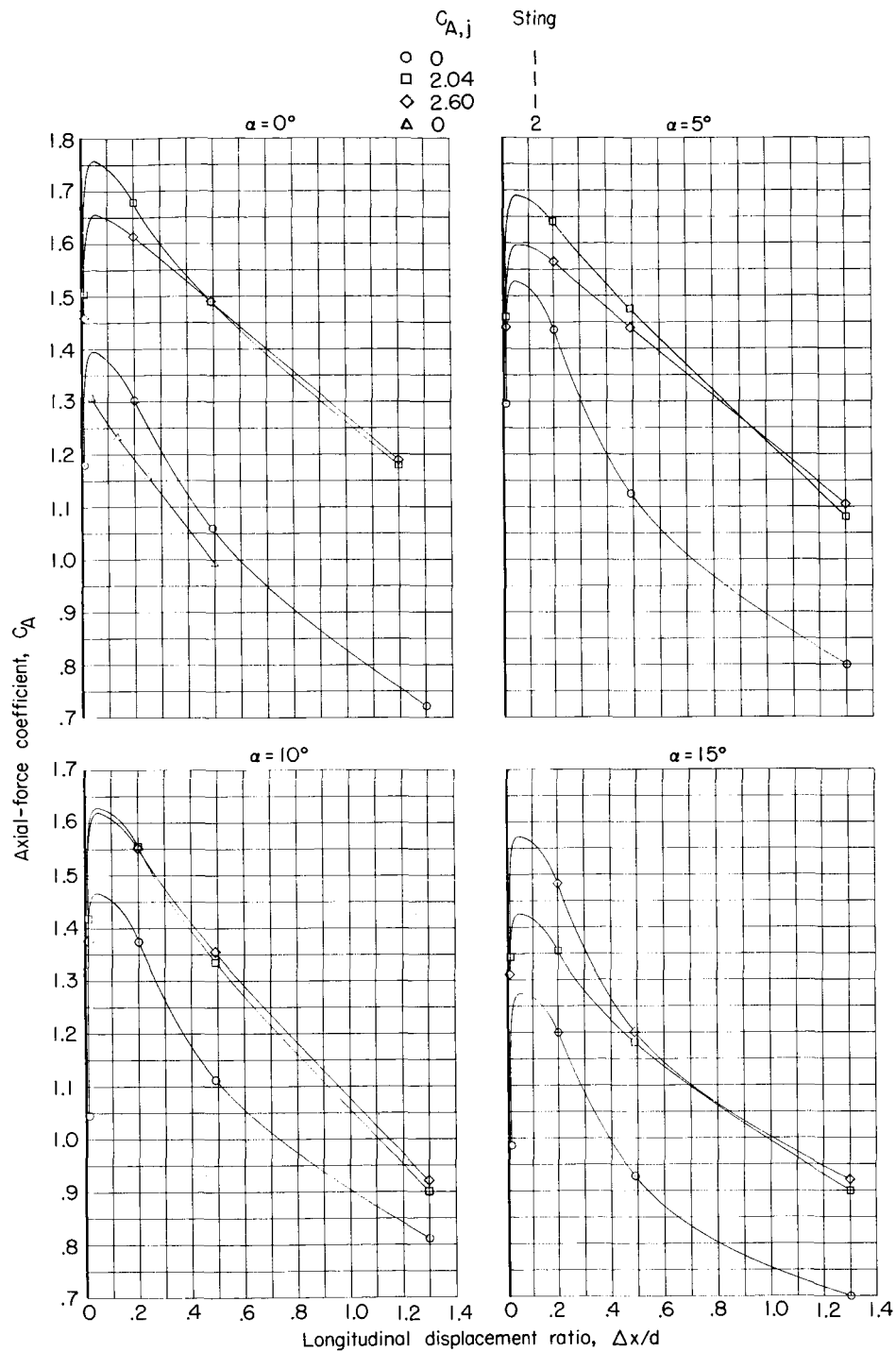
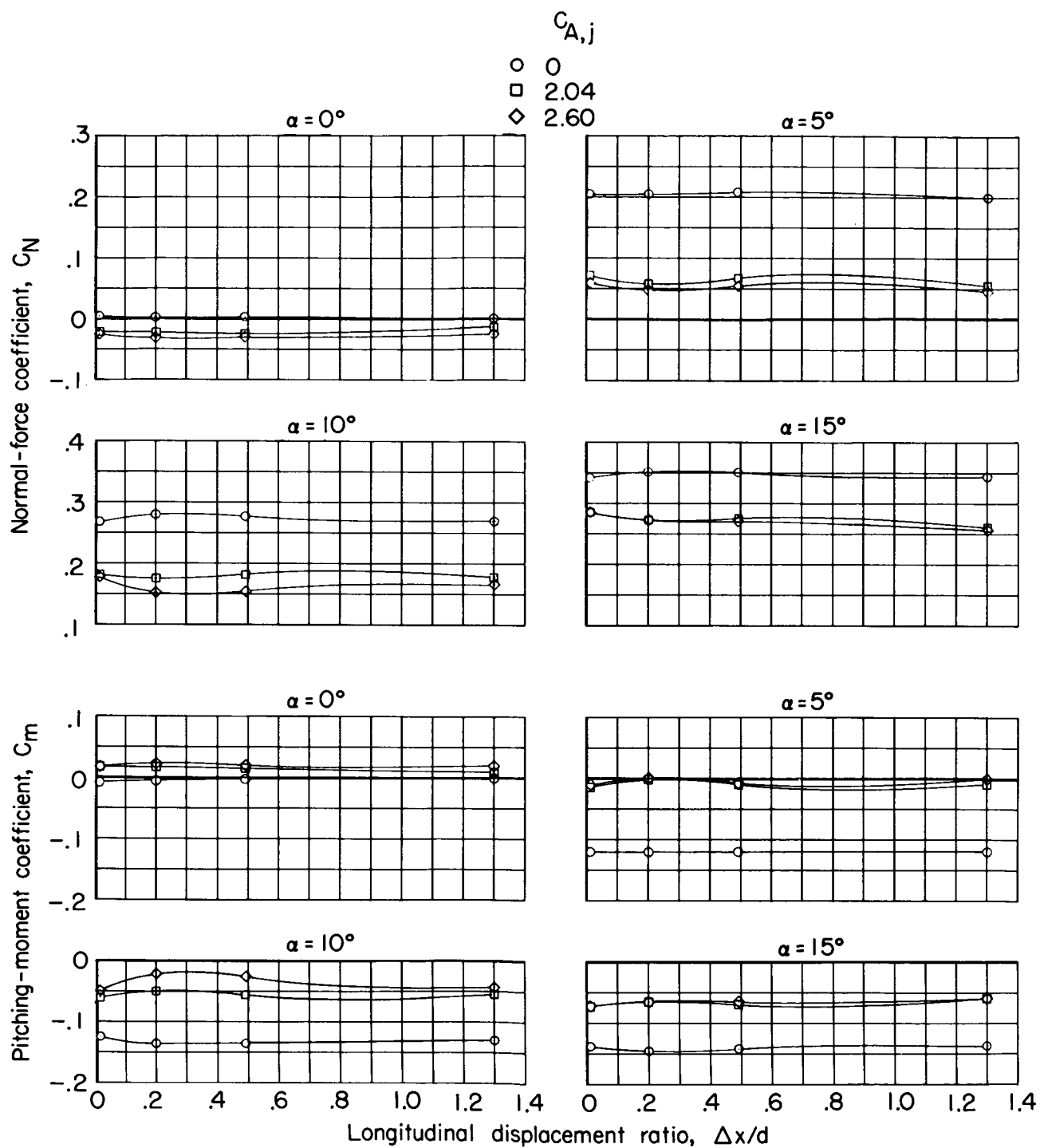
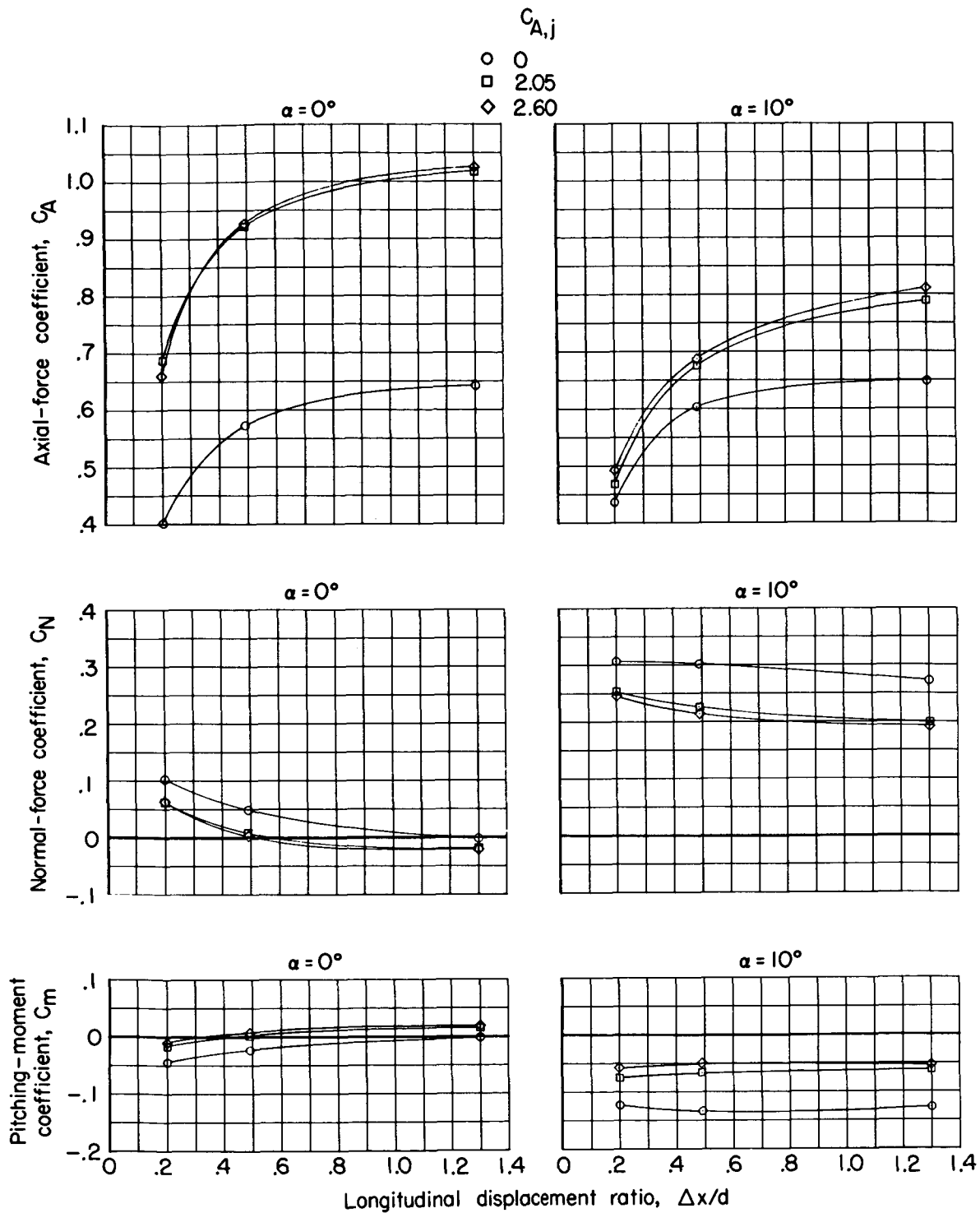


Figure 15.- Variation of axial-force, normal-force, and pitching-moment coefficients of command module with longitudinal displacement of service module; $M = 0.90$.



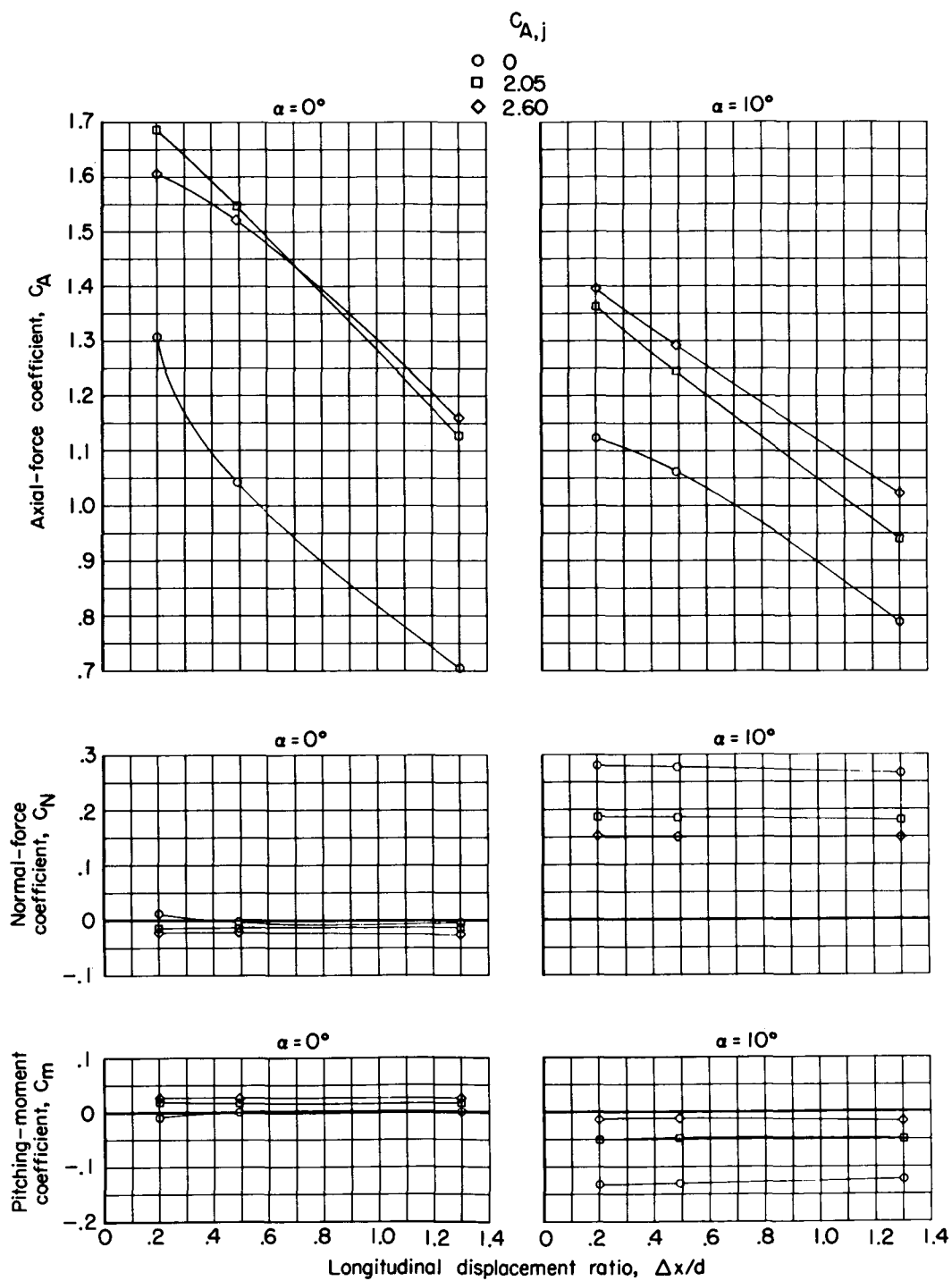
(b) Normal-force and pitching-moment coefficients; $\Delta z/d = 0$; $\Delta \alpha_s = 0^\circ$.

Figure 15.- Continued.



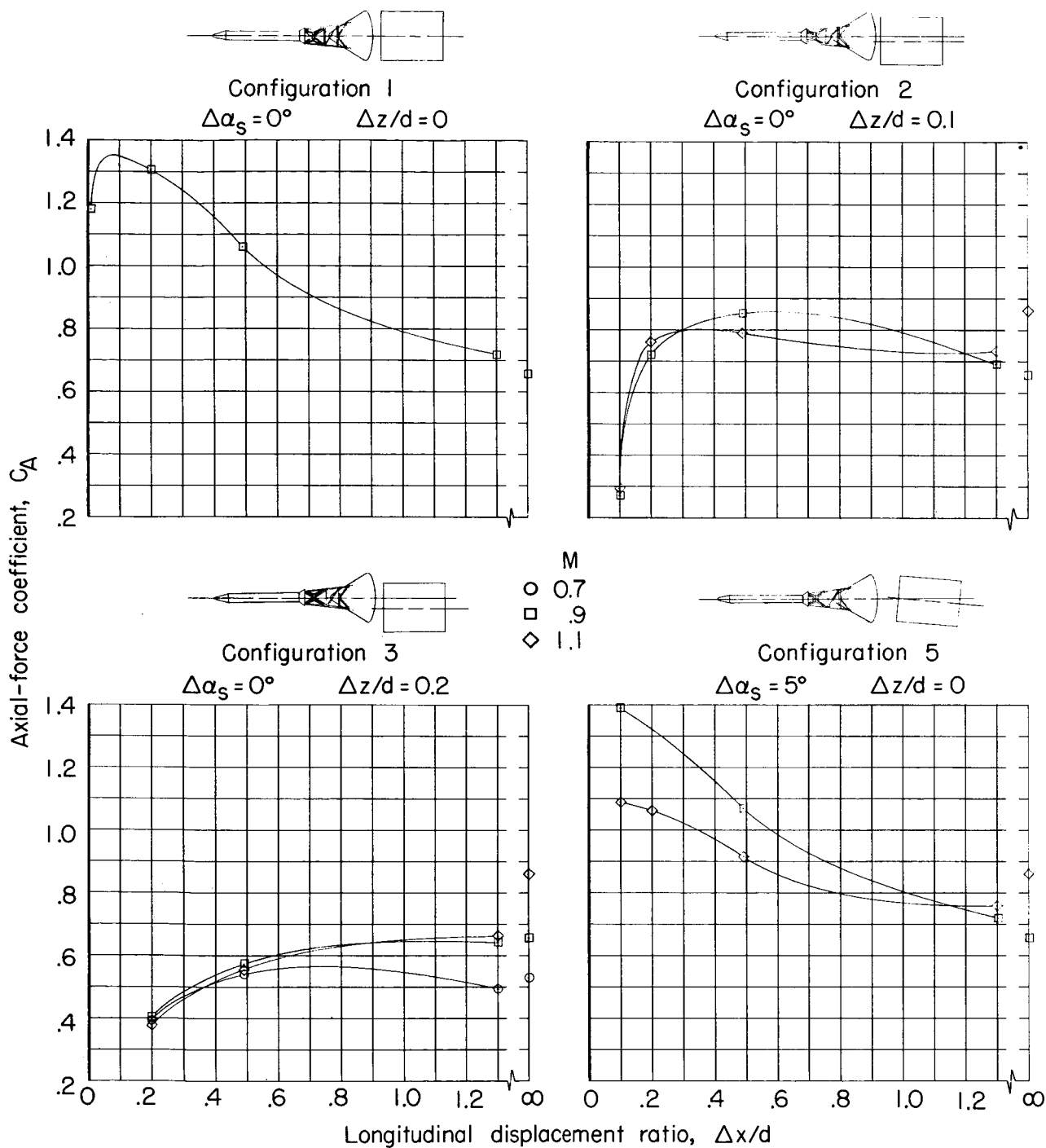
(c) Axial-force, normal-force, and pitching-moment coefficients; $\Delta z/d = 0.2$; $\Delta \alpha_s = 0^\circ$.

Figure 15.- Continued.



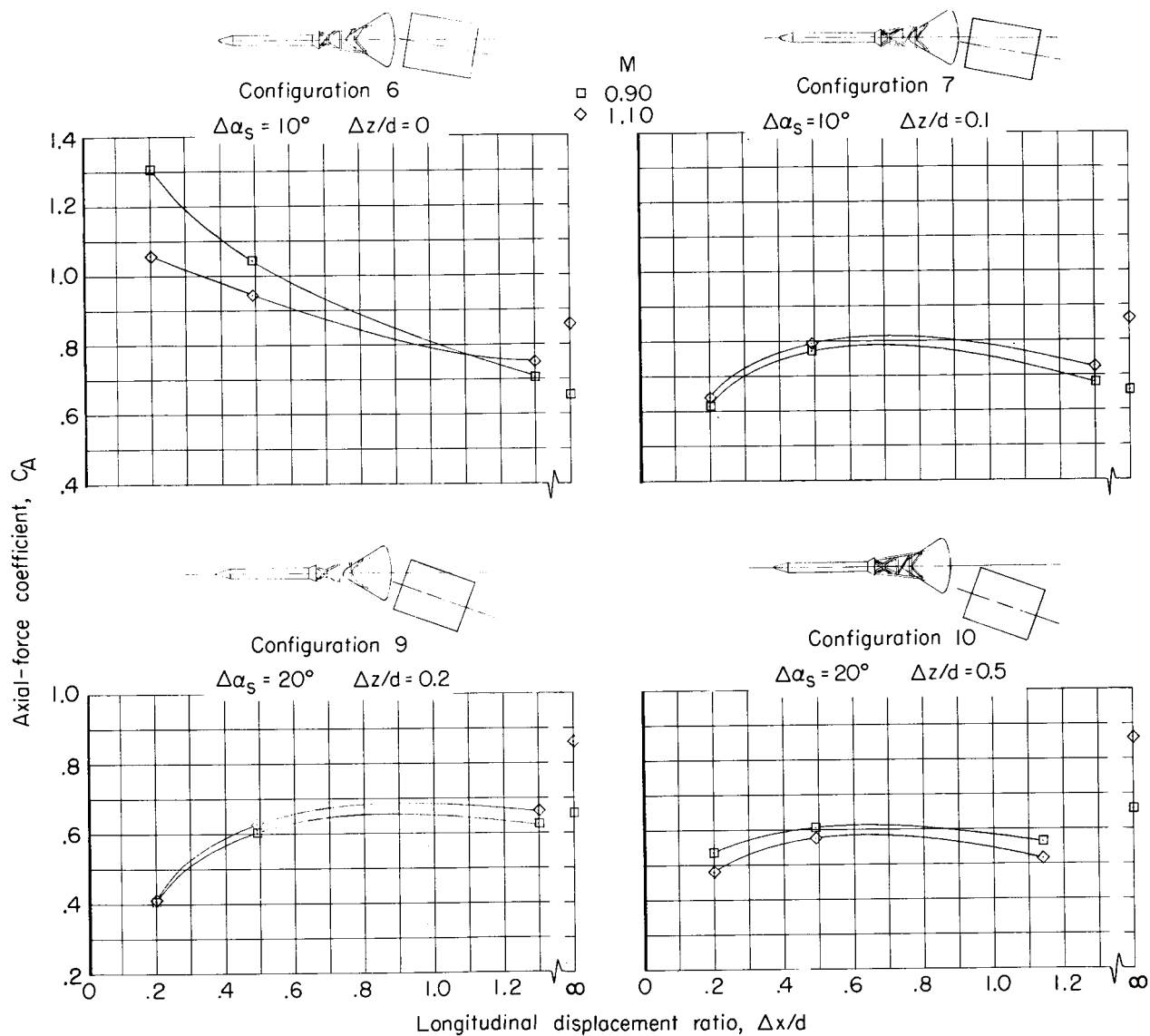
(d) Axial-force, normal-force, and pitching-moment coefficients; $\Delta z/d = 0$; $\Delta \alpha_s = 10^\circ$.

Figure 15.- Concluded.



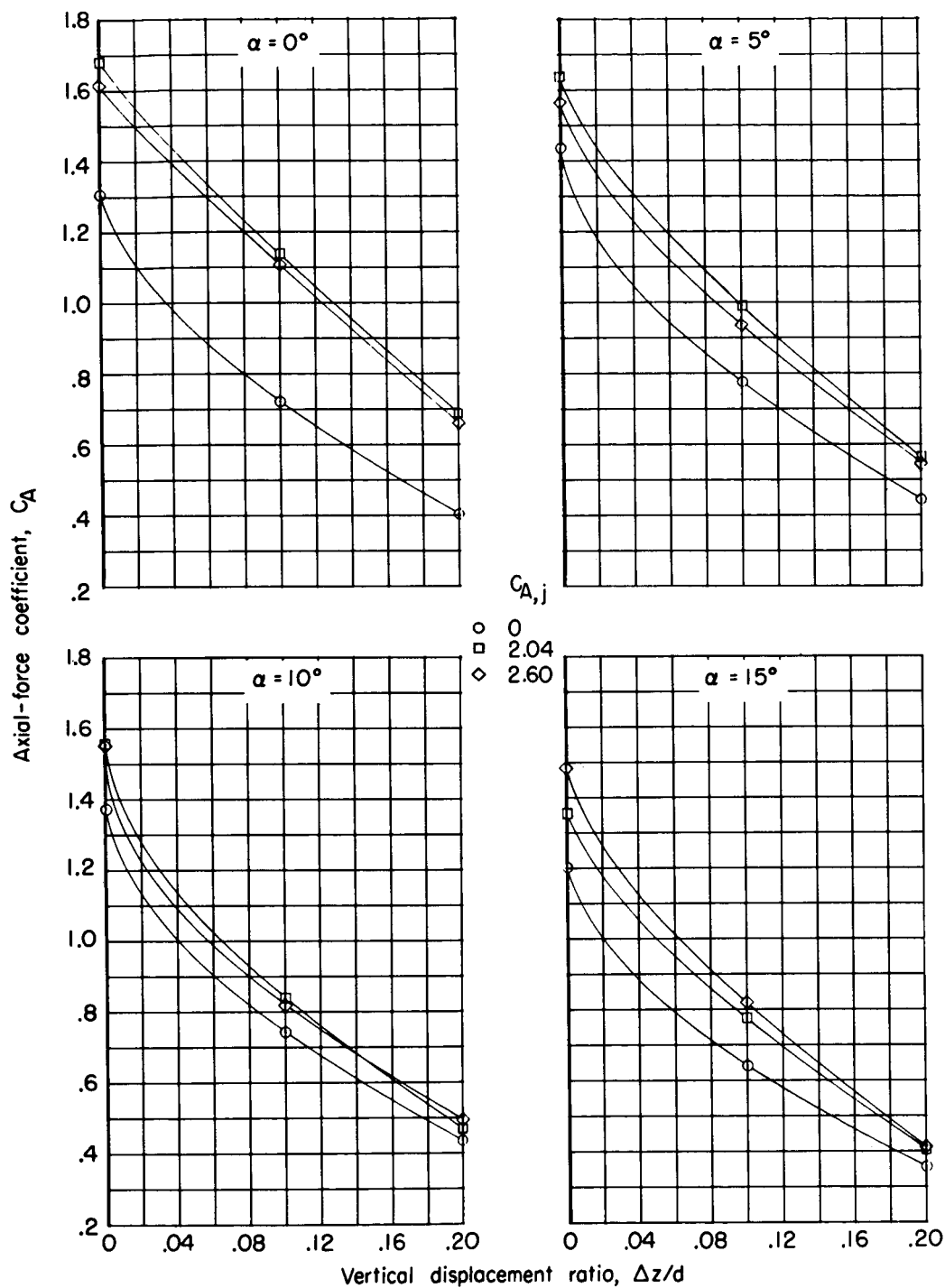
(a) Configurations 1, 2, 3, and 5.

Figure 16.- Variation of axial-force coefficient with fraction of longitudinal displacement of service module at several Mach numbers; $C_{A,j} = 0$; $\alpha = 0^\circ$. Isolated symbols indicate no service module.



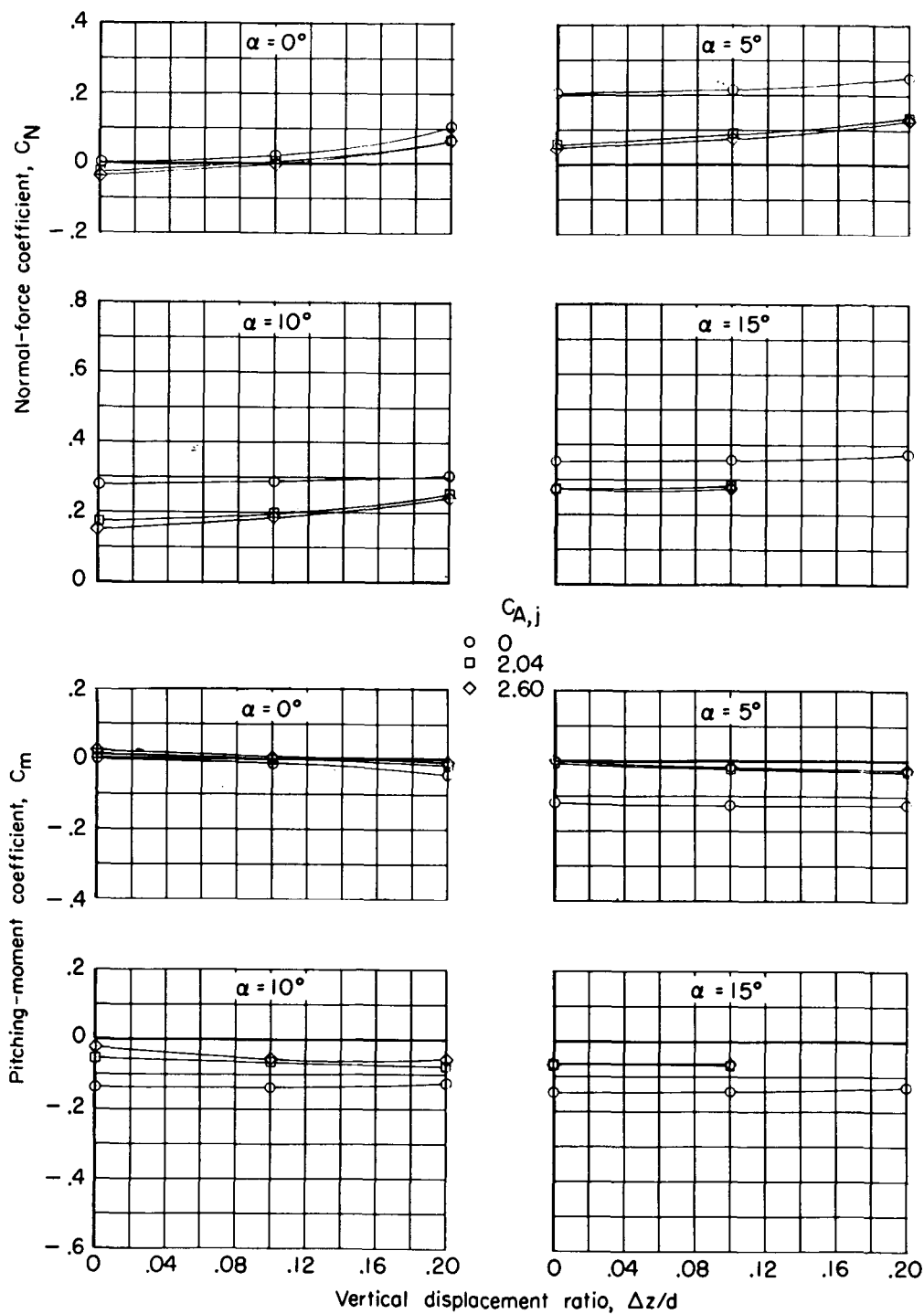
(b) Configurations 6, 7, 9, and 10.

Figure 16.- Concluded.



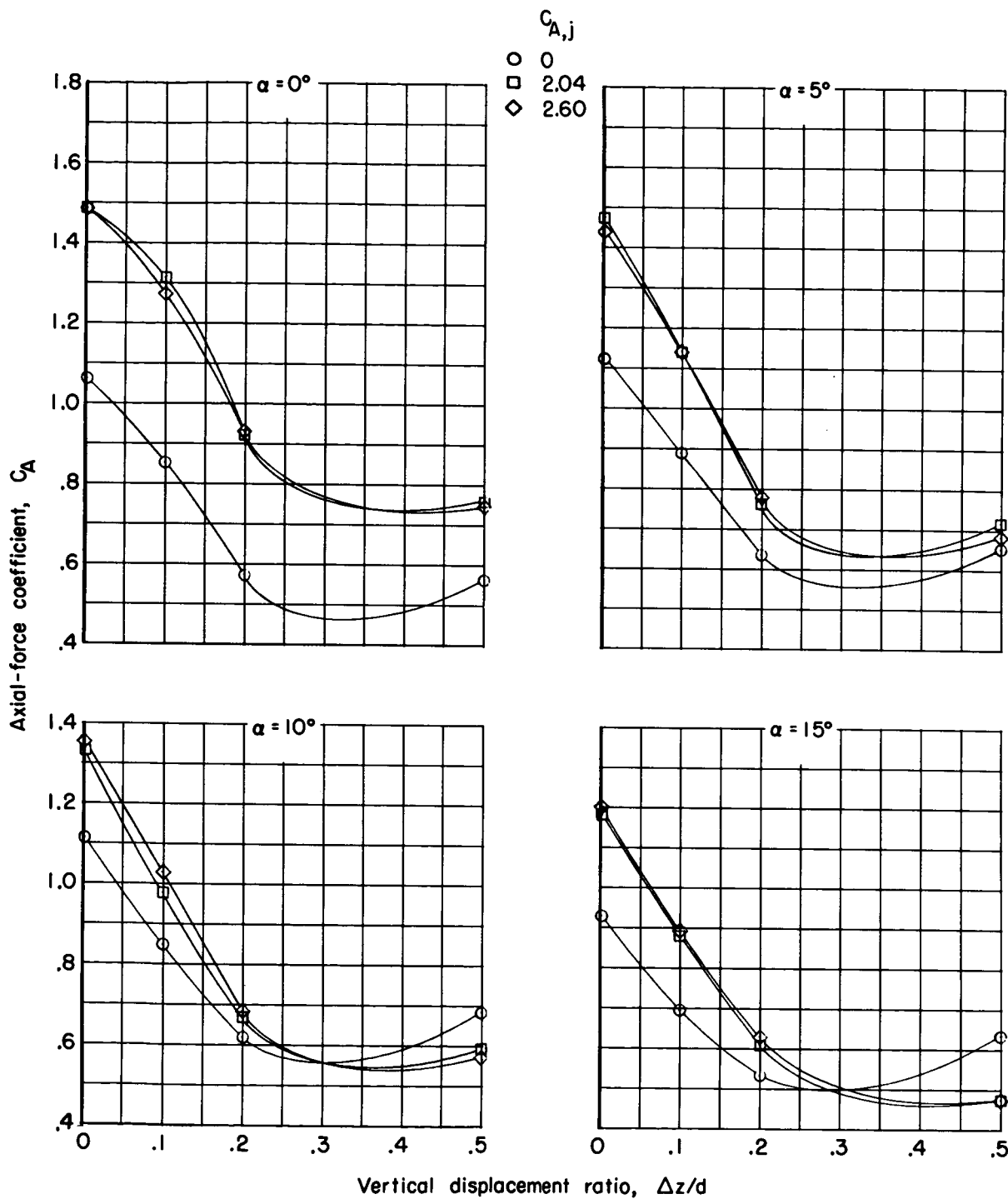
(a) Axial-force coefficient; $\Delta x/d = 0.20$.

Figure 17.- Effect of vertical displacement of service module on axial-force, normal-force, and pitching-moment coefficients of command module; $M = 0.90$; $\Delta \alpha_s = 0^\circ$.



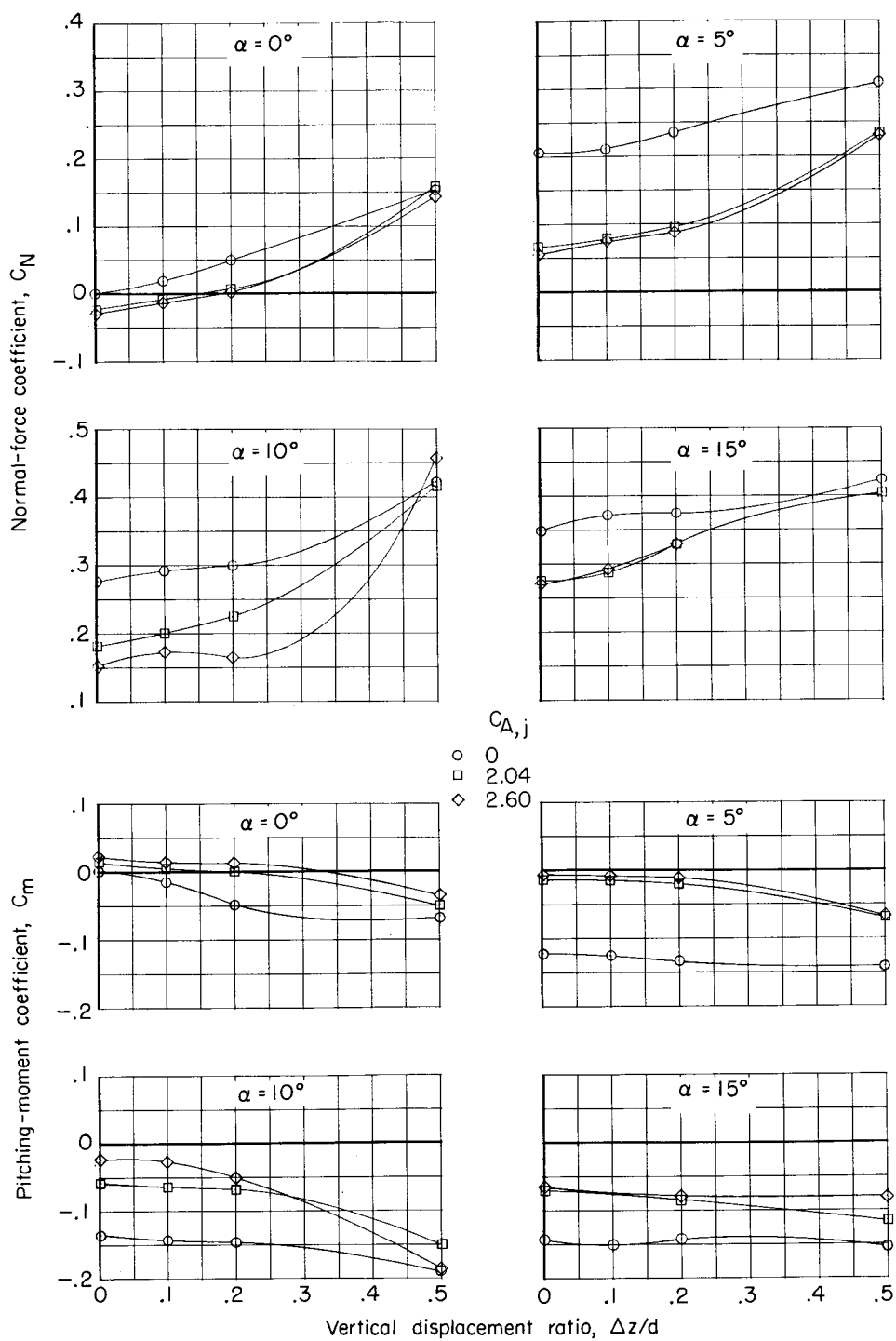
(b) Normal-force and pitching-moment coefficients; $\Delta x/d = 0.20$.

Figure 17.- Continued.



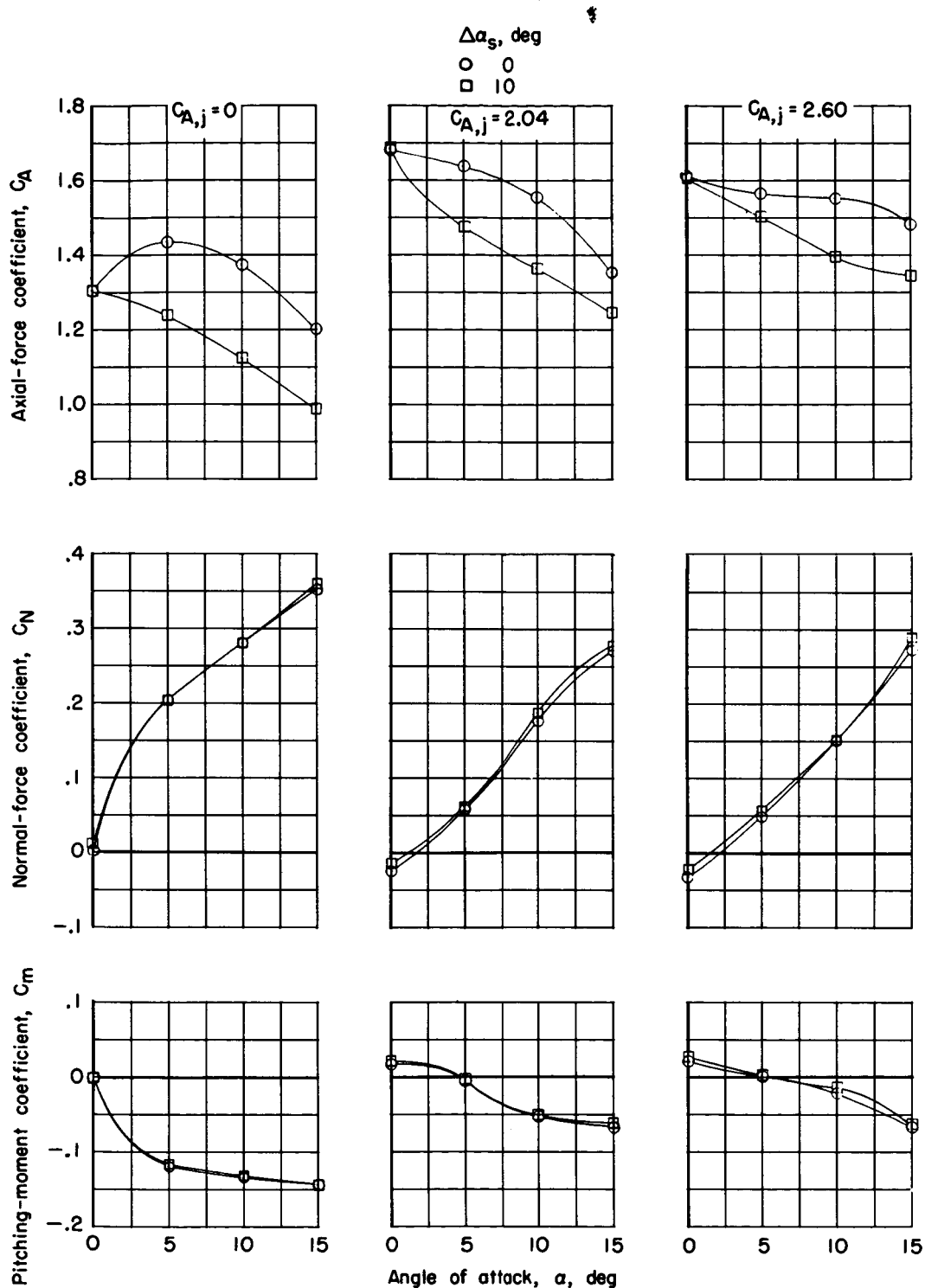
(c) Axial-force coefficient; $\Delta x/d = 0.49$.

Figure 17.- Continued.



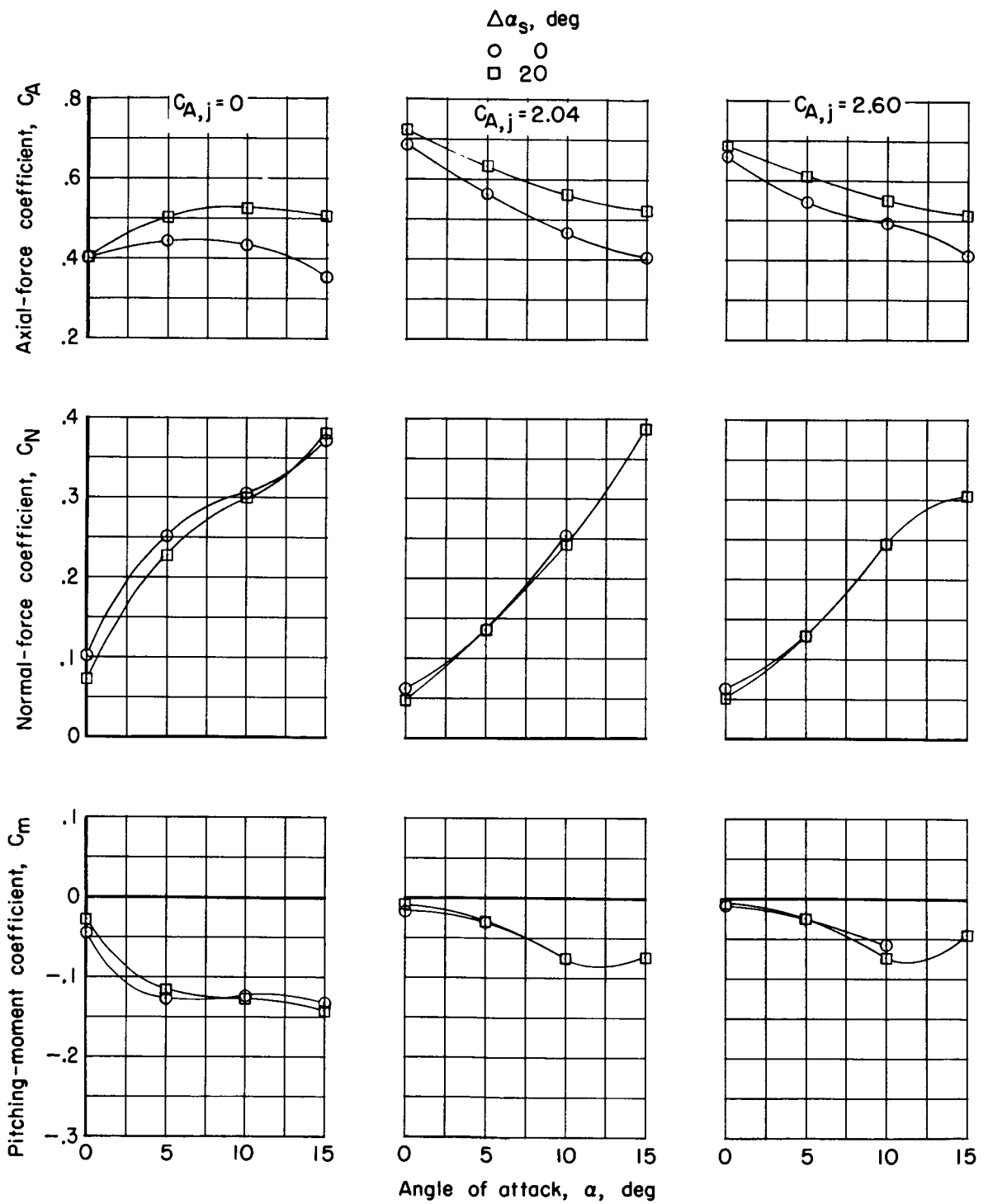
(d) Normal-force and pitching-moment coefficients; $\Delta x/d = 0.49$.

Figure 17.- Concluded.



(a) $\Delta z/d = 0$.

Figure 18.- Variation of axial-force, normal-force, and pitching-moment coefficients with angle of attack for several values of thrust coefficient and service module relative to angle of attack; $M = 0.90$; $\Delta x/d = 0.20$.



(b) $\Delta z/d = 0.20$.

Figure 18.- Concluded.